Geologic history of the summit of Axial Seamount, Juan de Fuca Ridge

Citation	Clague, D. A. et al. (2013), Geologic history of the summit of Axial Seamount, Juan de Fuca Ridge, Geochemistry Geophysics Geosystems, 14, 4403–4443. doi:10.1002/ggge.20240.
DOI	10.1002/ggge.20240
Publisher	American Geophysical Union
Version	Version of Record
Citable Link	http://hdl.handle.net/1957/46962
Terms of Use	http://cdss.library.oregonstate.edu/sa-termsofuse

Geochemistry Geophysics Geosystems G3

Article
Volume 14, Number 10
4 October 2013
doi: 10.1002/ggge.20240
ISSN: 1525-2027

Published by AGU and the Geochemical Society

Geologic history of the summit of Axial Seamount, Juan de Fuca Ridge

David A. Clague
Monterey Bay Aquarium Research Institute, Moss Landing, California, 95039, USA (clague@mbari.org)

Brian M. Dreyer
Institute of Marine SciencesUniversity of California, Santa Cruz, California, USA

Jennifer B. Paduan and Julie F. Martin
Monterey Bay Aquarium Research Institute, Moss Landing, California, USA

William W. Chadwick
CIMRS, Oregon State University, Newport, Oregon, USA

David W. Caress and Ryan A. Portner
Monterey Bay Aquarium Research Institute, Moss Landing, California, USA

Thomas P. Guilderson
Institute of Marine SciencesUniversity of California, Santa Cruz, California, USA

Center for Accelerator Mass Spectrometry, LLNL, Livermore, California, USA

Mary L. McGann
U.S. Geological Survey, Menlo Park, California, USA

Hans Thomas
Monterey Bay Aquarium Research Institute, Moss Landing, California, USA

David A. Butterfield
JISAO/PMEL, Seattle, Washington, USA

Robert W. Embley
PMEL, NOAA, Hatfield Marine Science Center, Newport, Oregon, USA

[1] Multibeam (1 m resolution) and side scan data collected from an autonomous underwater vehicle, and lava samples, radiocarbon-dated sediment cores, and observations of flow contacts collected by remotely operated vehicle were combined to reconstruct the geologic history and flow emplacement processes on Axial Seamount's summit and upper rift zones. The maps show 52 post-410 CE lava flows and 20 precaldera lava flows as old as 31.2 kyr, the inferred age of the caldera. Clastic deposits 1–2 m thick accumulated on the rims postcaldera. Between 31 ka and 410 CE, there are no known lava flows near the summit. The oldest postcaldera lava (410 CE) is a pillow cone SE of the caldera. Two flows erupted on the W rim between ~800 and 1000 CE. From 1220 to 1300 CE, generally small eruptions of plagioclase phyric, depleted, mafic lava occurred in the central caldera and on the east rim. Larger post-1400 CE eruptions produced inflated lobate flows of aphyric, less-depleted, and less mafic lava on the upper rift zones and in the N and S caldera. All caldera floor lava flows, and most uppermost rift zone flows, postdate 1220 CE. Activity shifted from the central caldera to the upper S rift outside the caldera, to the

N rift and caldera floor, and then to the S caldera and uppermost S rift, where two historical eruptions occurred in 1998 and 2011. The average recurrence interval deduced from the flows erupted over the last 800 years is statistically identical to the 13 year interval between historical eruptions.

Components: 29,629 words, 20 figures, 2 tables.

Keywords: Axial Seamount; Juan de Fuca Ridge; geologic; mapping; lava flows.

Index Terms: 3035 Midocean ridge processes: Marine Geology and Geophysics; 3017 Hydrothermal systems: Marine Geology and Geophysics; 3045 Seafloor morphology, geology, and geophysics: Marine Geology and Geophysics; 3094 Instruments and techniques: Marine Geology and Geophysics; 8424 Hydrothermal systems: Volcanology; 8429 Lava rheology and morphology: Volcanology; 0450 Hydrothermal systems: Biogeosciences; 1034 Hydrothermal systems: Geochemistry; 3616 Hydrothermal systems: Mineralogy and Petrology; 4832 Hydrothermal systems: Oceanography: Biological and Chemical; 8135 Hydrothermal systems: Tectonophysics; 9355 Pacific Ocean: Geographic Location.

Received 22 March 2013; **Revised** 26 July 2013; **Accepted** 4 August 2013; **Published** 4 October 2013.

Clague, D. A. et al. (2013), Geologic history of the summit of Axial Seamount, Juan de Fuca Ridge, *Geochem. Geophys. Geosyst.*, *14*, 4403–4443, doi:10.1002/ggge.20240.

1. Introduction

[2] Submarine volcanoes are difficult to study compared to more accessible subaerial volcanoes, which has resulted in poor understanding of their geologic histories. Two impediments to progress have been technological limitations in obtaining synoptic high-resolution mapping of volcanic areas and the nearly complete lack of absolute ages to constrain the timing of events. Studies to conduct geologic mapping along young spreading ridges using ship-based sonars, towed side scan and cameras, and bottom observations from submersibles have been carried out since the late 1970s [e.g., *Ballard and van Andel*, 1977; *Ballard et al*., 1979; *Crane and Ballard*, 1981]. Techniques were applied for several decades, largely to define flow boundaries of historical flows along the spreading ridges [e.g., *Embley et al*., 1991, 1995, 1999, 2000; *Fox et al*., 1992; *Haymon et al*., 1993; *Chadwick et al*., 1995, 1998, 2001, 2002; *Chadwick and Embley*, 1994; *Embley and Chadwick*, 1994; *Sinton et al*., 2002; *Soule et al*., 2005, 2007, 2009; *Fundis et al*., 2010; *Goss et al*., 2010; *Fornari et al*., 2004, 2012; *White et al*., 2000]. High-resolution bathymetric mapping techniques, similar to those utilized in this study, combined with submersible observations have recently been done on small parts of the East Pacific Rise [*Cormier et al*., 2003; *Ferrini et al*., 2007; *Yeorger et al*., 2007] and along two portions of the Galapagos Spreading Center [*Colman et al*., 2012; *White et al*., 2008]. Such detailed mapping is needed to determine fundamental characteristics of lava flows, such as area, length, flow morphologies, structure, spatial distribution of the flow morphologies, and location of eruptive fissures. These basic observations [*Perfit and Chadwick*, 1998] provide the framework to understand, for example, eruption frequencies and dynamics, spatial and temporal changes in magmatic processes and activity, changes in magmatic plumbing systems and magma sources, and the interplay of tectonism and magmatism along ridges.

[3] The flows from the 2011 eruption at Axial Seamount are the only ones mapped with both pre-eruption and posteruption 1 m resolution bathymetric data. These data were used to map the extent and thicknesses, and hence estimate the volume erupted for the flows nearest the summit [*Caress et al*., 2011, 2012a]. Even our knowledge of the 2011 eruption is limited by a lack of pre-eruption high-resolution mapping where pillow flows are inferred to have constructed a tall ridge deep on the S rift zone. Prior efforts at determining flow extents and volumes have been limited by the low resolution of shipboard surveys used in the comparisons, as well as poor, pre-Global-positioning system navigational control for most of the pre-eruptive maps.

[4] Even with high-resolution mapping data, the frequency of eruptions, the timing of major events such as caldera formation, and rates of change in lava chemistry remain speculative without absolute time constraints. Previous studies have focused on Ar-Ar analyses [e.g., *Clague et al*., 2009b], U-Th systematics [e.g., *Rubin and*

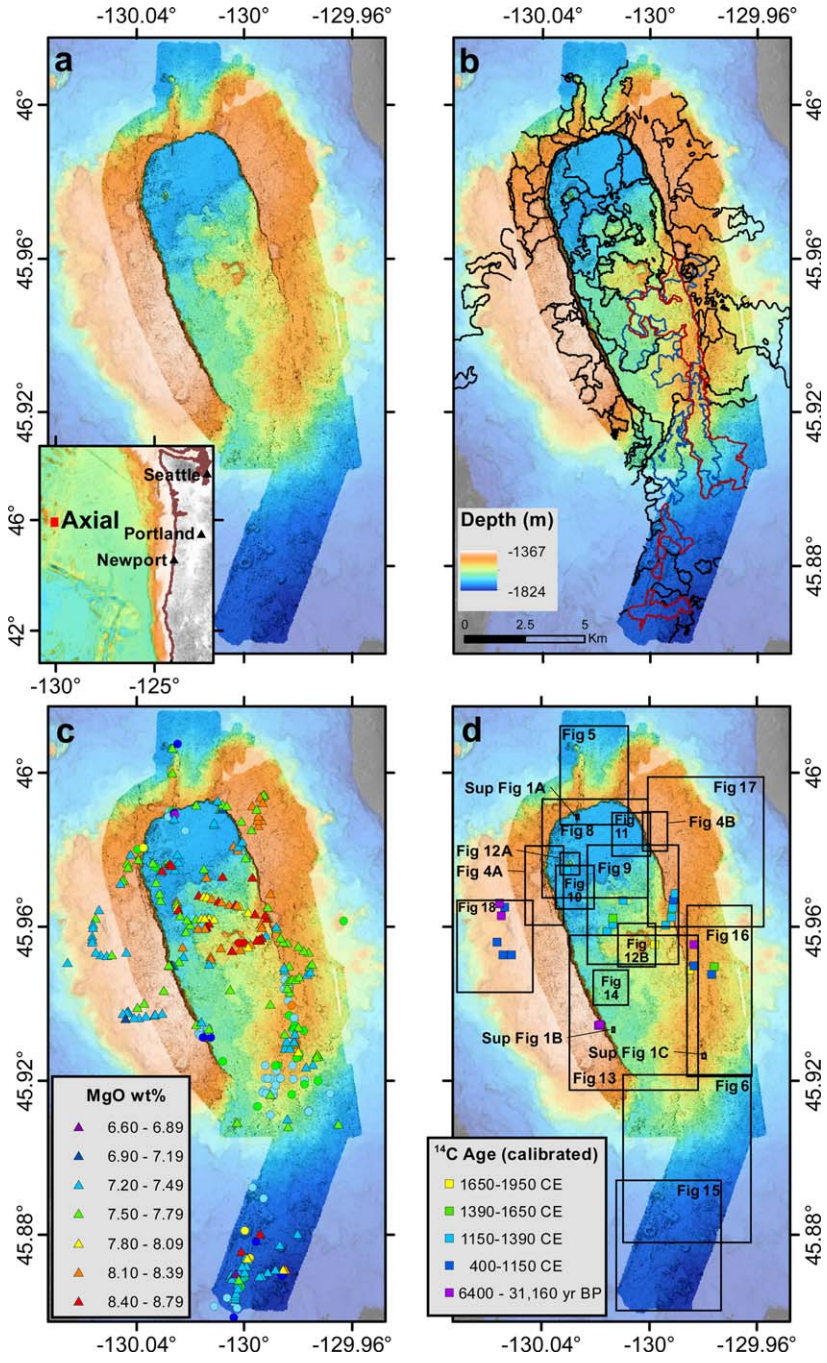

Figure 1. (a) Summit of Axial Seamount showing area mapped at 1 m resolution using the MBARI autonomous underwater vehicle (AUV) *D. Allan B*. in 2006–2011. Background 20 m resolution shipboard bathymetry is shown using the same histogram-equalized −1825 m (blue) to −1367 m (orange) color ramp, but faded. In all subsequent figures, depths shallower and deeper than the color ramp depth range are white and black, respectively. Red dot in inset shows the location of Axial Seamount 460 km offshore the NW United States. (b) Same map with contacts between flow units shown in black, except the 2011 flow [*Caress et al*., 2012a] shown in blue (also used in subsequent figures to show areas that were covered by the 2011 flows), and the 1998 flows [*Chadwick et al*., 2013] shown in red. (c) Same map showing lava sample locations, symbolized for glass MgO contents on a normalized volatile-free basis. New samples from this study are shown as triangles and published analyses of samples from *Chadwick et al*. [2005] are shown as filled circles. (d) Same map showing (1) the locations of cores that have been dated using accelerator mass spectrometry (AMS) radiocarbon dating of foraminifera and (2) the locations and extents of subsequent figures as labeled boxes. Ages are color coded into five ranges as indicated in the key. The same symbols are used throughout the paper.

Macdougall, 1990, 2012; *Goldstein et al*., 1992; *Volpe and Goldstein*, 1993] that give 10–200 kyr time constraints, or ^{226}Ra, ^{210}Pb or ^{210}Po analyses that provide detailed insight into eruptions in the years to centuries timeframe [e.g., *Rubin et al*., 2005; *Bergmanis et al*., 2007].

[5] On land, radiocarbon dating of charcoal collected from beneath lava flows is a routine method to determine the ages of lava flows [e.g., *Rubin et al*., 1987]. On the seafloor, unfortunately, carbonaceous material from beneath the edges of lava flows is nearly impossible to access. Sediment containing foraminifera composed of calcite, however, accumulates on top of the flows if the site is located shallower than the calcium carbonate compensation depth [*Broecker et al*., 1990; *Stuiver and Braziunas*, 1993; *Clague et al*., 2011b]. We have collected this accumulated sediment in short cores using ROVs.

[6] In this study, we have combined 1 m resolution multibeam bathymetric data collected by an autonomous underwater vehicle (AUV) with radiocarbon ages [e.g., *Broecker et al*., 1990] of foraminifera on top of lava flows, chemistry of lava samples, and visual observations collected by remotely operated vehicles (ROV) to map the summit of Axial Seamount on the Juan de Fuca Ridge. Lava flow boundaries were defined using the high-resolution bathymetry, visual observations of flow contacts, the mineralogy and major element compositions of glasses from lava flows within the mapped area, and to a lesser degree, side scan and backscatter data. We utilize published glass compositions of 172 lava samples located within the mapped region [*Chadwick et al*., 2005] and glass from 236 new lava samples collected by ROVs using the high-resolution maps to guide the sampling. A companion paper examines the 1998 eruption and flows in detail [*Chadwick et al*., 2013]. Another companion paper examines the petrologic evolution of Axial summit lavas using isotopic and trace element data of a subset of the samples from this study (*Dreyer*, 2013) and places the lava compositions into a time framework based on the age data presented here.

[7] The combination of high-resolution AUV mapping data and observations from ROVs, relative and absolute age control, and flow compositions enables us to reconstruct the geologic history of the summit of Axial Seamount on the Juan de Fuca Ridge, much like geologists routinely do on subaerial volcanoes.

2. Geologic Setting

[8] The tectonic setting of Axial Seamount on the Juan de Fuca mid-ocean ridge has been described in detail by *Karsten and Delaney* [1989] and *Desonie and Duncan* [1990], and reviewed more recently by *Chadwick et al*. [2005, 2010]. Likewise, the morphology of the seamount has been described in detail in *Zonenshain et al*. [1989] and *Embley et al*. [1990] based on shipboard bathymetry, side scan data, and observations from numerous submersible and remotely operated vehicles (ROV) dives. Recent work at Axial Seamount has focused on the eruptions in 1998 [*Chadwick et al*., 2009b, 2013] and 2011 [*Chadwick et al*., 2012; *Dziak et al*., 2012; *Caress et al*., 2012b] and on the fluids and biology of hydrothermal vents [summarized in *Butterfield et al*., 2004].

[9] The summit of Axial Seamount is located at 45°57′N, 130°01′W near the center of the Axial segment of the Juan de Fuca Ridge. The summit has an oval horseshoe-shaped ~3 km × 8 km caldera trending 170° that is deepest to the NW and whose SE rim is buried by lava flows (Figure 1a). *Embley et al*. [1990] compared it to other calderas on basaltic volcanoes. The caldera floor gradually shoals to the SSE. The spatial configuration of the two rift zones and the caldera, including the rifts curving toward each other in their overlap zone, are similar to overlapping spreading ridges with the caldera between the overlapping ridges, as discussed by *Embley et al*. [1990].

[10] The S rift zone plunges from about 1530 m depth at the inferred (buried) location of the S rim of the caldera (Figure 2) to a depth of about 2400 m over a distance of ~50 km, where it overlaps with the Vance segment of the Juan de Fuca Ridge to the E. Likewise, the N rift plunges from about 1505 m near the N caldera rim to a depth of about 2200 m over ~50 km where it overlaps with the CoAxial segment of the Juan de Fuca Ridge to the east (see depth profile along entire Juan de Fuca Ridge in *Chadwick et al*. [2005, Figure 1]).

3. Methods

3.1. Autonomous Underwater Vehicle Mapping

[11] The MBARI AUV *D. Allan B*. mapped the summit and upper S rift of Axial Seamount during

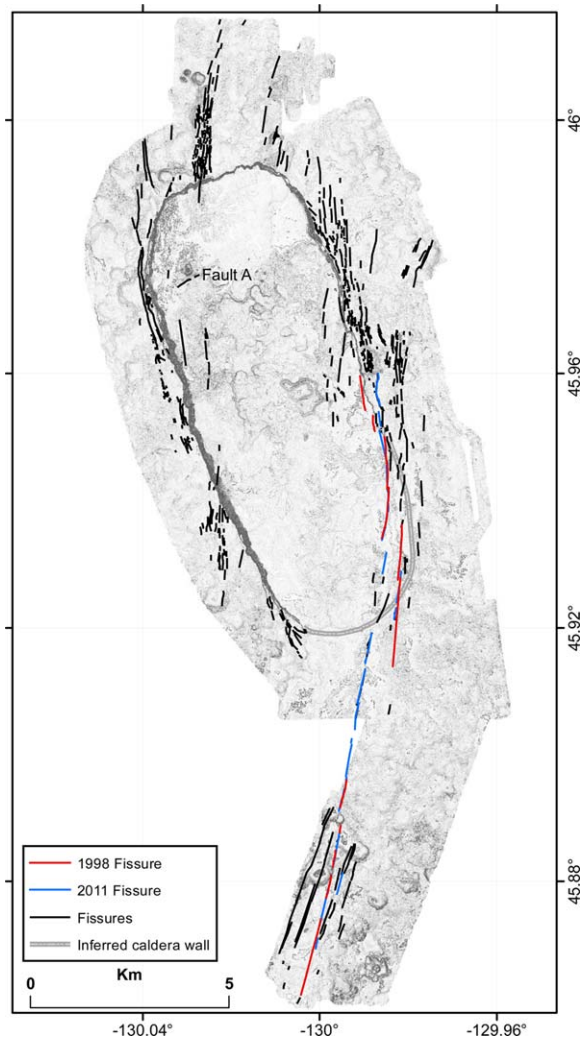

Figure 2. The AUV bathymetry is shown in grayscale with identified fissures indicated in black, 1998 fissures in red [*Chadwick et al*., 2013], and 2011 fissures in blue [*Caress et al*., 2012a]. The cluster of fissures north of the caldera at about 130°1.6′W marks the North Rift Zone with an orientation of about 005°. Fissures of similar orientation occur on the NW caldera floor and cut the west rim. Fissures at the south end of the caldera occupy a much wider zone and have an orientation of about 020°. These fissures wrap around the SE caldera, where not buried by young flows, to become nearly N-S on the E rim and splay to similar NE-SW trends of the south rift on the lower E flank. Fault A is discussed in the text. Gray and white dashed line indicates the inferred location of the buried south caldera wall [*Chadwick et al*., 2013]. Fissures in all subsequent figures are shown in red.

five cruises between 2006 and 2011. The high-resolution mapping was largely confined to the summit, extending only 2.8 km down the N rift and 6.7 km down the S rift. The final navigation is accurate in a relative sense to 1 m, in an absolute sense to 35 m (the lateral resolution of the EM302 bathymetry), and has a vertical precision of 0.1 m. Early results of this mapping program were presented by *Clague et al*. [2007, 2011b] and *Caress et al*. [2007].

[12] The AUV *D. Allan B*. is described in *Caress et al*. [2008, 2012a] and *Clague et al*. [2011a] and additional details about the vehicle and the post-collection processing of the data are included in supporting information[1]1. The extent of the pre-2011 AUV mapping coverage is shown in Figure 1, with outlines showing where subsequent map figures are located. Legends for symbology used in subsequent figures are also shown in Figure 1.

[13] The AUV bathymetry is the primary data used to draw flow boundaries, as shown in Figure 1b. The *side scan* data collected during the mapping missions were also used to identify young lava flows with minimal sediment on the caldera rims by their brightness in the side scan imagery. Young lava flows with thin sediment cover can also be identified, at much lower resolution, using *backscatter* derived from amplitude of shipboard multibeam sonar data, as utilized beyond our AUV coverage.

3.2. Sampling and Lava Analyses

[14] Bottom observations and sample collection used four different ROVs during 2005–2007, 2009, and 2011, as explained in detail in supporting information 2.1 and shown on supporting information Figure S1. The samples include those collected by ROV plus 19 wax-tip rock-corer samples and a sample recovered in the nosecone of the mapping AUV when it accidentally impacted the bottom during a survey in 2007. In total, 236 new lava samples, first presented here, were recovered and analyzed, and are well located on the underlying 1 m bathymetry. These samples add to the already large collection of samples recovered with the ROV *ROPOS* during NeMO cruises between 1998 and 2001, of samples collected by *Pisces IV* and *Alvin* submersibles in 1987 and 1988, and recovered using the German GTVG grab sampler from the R/V *Sonne* in 1996 [*Chadwick et al*., 2005]. Of those previously collected 309 samples, 172 are from within the AUV mapped region; those outside will not be discussed further. The previous sample collections were mainly from flows near the hydrothermal vent fields, and thus four lava flows are represented by 127 analyzed samples [*Chadwick et al*., 2005], whereas our new samples are more widely distributed over the

caldera floor and caldera rims (Figure 1c), with some samples from the near-vertical caldera walls.

[15] Lava samples were collected using the manipulators on the ROVs and stowed in partitions on each vehicle. For *Tiburon* and *Doc Ricketts* dives, up to 31 rock samples were collected per dive. Care was taken to photo-document each sample before stowing it and these photographs were then used as samples were removed from the vehicles to minimize sample misidentification.

[16] Glass rinds on all lava samples were analyzed by electron microprobe as outlined in supporting information 2.2 and the results are presented in supporting information Table S1 for new samples and for four glass standards. The International Geologic Sample Numbers (IGSN) are listed in supporting information Table S1 and the data have been submitted to the Earthchem.org Petrological Database (PetDB). Supporting information Table S2 lists sample numbers and their locations for published glass analyses of samples that are within our AUV mapped region [*Chadwick et al*., 1995]. In both these tables, each sample is assigned to a flow unit, based on its location on the high-resolution map as described in the results section below.

[17] Critical dive observations consist of identifying flow morphology, locations of flow contacts, sediment cover, and relative flow ages at contacts. Dive tracks for submersible and ROV dives that collected samples and observations used in this study are shown on supporting information Figure S1, which excludes dives exclusively at the hydrothermal vent fields.

3.3. Sediment Coring and Radiocarbon Dating

[18] Most flows on the rim of the caldera and some flows on the caldera floor underlie sediment deposits thick enough to collect in cores (<1 m long) from ROVs. These clastic sediments are predominantly composed of glass shards produced during pyroclastic eruptions [*Clague et al*., 2003, 2009; *Sohn et al*., 2008], but include planktic (e.g., radiolaria, diatoms, and foraminifera tests), benthic (e.g., foraminifera tests and sponge spicules), and hydrothermal components; they are referred to here as clastic deposits. The clastic deposits on the rim, first recognized and sampled by *Zonenshain et al*. [1989], are thicker and commonly contain more hydrothermal material than the deposits on the caldera floor. Flow ages were determined from foraminifera hand picked from the basal cm of 30 cm or 1 m cores collected by the ROVs *Tiburon* and *Doc Ricketts*, as explained in supporting information 2.3. Chronological control was based on radiocarbon analysis via accelerator mass spectrometry. Conventional radiocarbon ages were calibrated in calendar years for samples more recent than 400 CE or, for older samples, to calibrated (cal) years (yr) before present (BP), where present is 1950. The radiocarbon data and marine calibrations made using Calib 6.1.0 [*Stuiver and Reimer*, 1993] are presented in Table 1. Applied ΔR-factors used in the calibrations are listed in the table and explained in supporting information 2.4. Radiocarbon analyses of the carbonate skeletons or shells of a dozen living benthic animals were analyzed to confirm the age of the bottom water in which benthic foraminifera lived (supporting information Table S3). These results are plotted with hydrocast data as a function of depth (supporting information Figure S2). Comparison of calibrated ages determined from planktic/benthic foraminifera pairs from Juan de Fuca Ridge were compared (supporting information Figure S3) to verify that reservoir ΔR-factors utilized in the radiocarbon calibrations are consistent. Radiocarbon analyses from 32 cores provide minimum ages of eight flows on the caldera floor and 10 on the rim (Table 1, Figure 1d). The ± -cited are 2σ errors determined from the median probability age of the ^{14}C analysis and do not include any estimate of geologic uncertainty.

[19] The calibrated ages in Table 1 are minimum ages for the underlying lava flows for a number of reasons. The primary one is that the oldest sediment on top of the flow may not have been sampled depending on whether the deepest pocket of sediment was cored and recovered. The foraminifera were also extracted from a 1 to 2 cm portion of the core, and so their age must be younger than the age at the basalt/clastic deposit interface. In addition, bioturbation or other physical mixing of the clastic deposits can reduce the apparent age of the basal portion of the core. For short cores, this may become a significant effect, but for all cores, some mixing takes place and younger introduced components are included in the basal slice, reducing the age of the bulk sample. The mixed layer at Axial Seamount is apparently thinner than at other mid-ocean ridge sites we have similarly sampled and analyzed, perhaps because the abundant sharp glass shards in the sediment discourages benthic animal burrowing. The generally subdued topography minimizes the likelihood of transport by gravity flows [*Van Andel and Komar*, 1969].

Table 1. Radiocarbon Analytical Data and Calibration[a]

Sample Number	Flow Unit	CAMS #	Type	Latitude	Longitude	Depth (m)	$d^{13}C$	Fraction Modern	±	$D^{14}C$	±	^{14}C Age	±	Reservoir Correction (yr)	Marine Δ R-Factor (yr)	Calibrations Based on Program Calib 6.1.0 [*Stuivier and Reimer*, 1993] 1σ Low (cal yr BP)	1σ High (cal yr BP)	1σ Prob.	Avg. 1σ (cal yr BP)	2σ Low (cal yr BP)	2σ High (cal yr BP)	2σ Prob.	Avg. 2σ (cal yr BP)	Median Prob. (cal yr BP)	Median Prob. (CE)	+2σ (yr)	−2σ (yr)
Axial Summit-Caldera Floor																											
D71-PC72: 17–18 cm	Ng2	147,450	P	45.97459	−130.03075	1566	1	0.8311	0.0030	−168.9	3.0	1485	30	800	400	625	673		649	590	707	0.967	649	**650**	**1300**	**57**	**60**
																				565	585	0.033	575				
D74-PC17: 10–11 cm	Nh2	147,451	P	45.96677	−130.00971	1536	1	0.8320	0.0039	−168.0	3.9	1480	40	800	400	612	682		647	554	712		633	**645**	**1305**	**67**	**91**
D74-PC56: 12–13 cm	Ne	147,452	P	45.95535	−129.99801	1531	1	0.8786	0.0030	−121.4	3.0	1040	30	800	400	255	310		283	228	403	0.999	316	**286**	**1664**	**117**	**58**
																				153	156	0.001	155				
D74-PC60: 15–16 cm	Nk	147,453	P	45.96054	−129.99392	1525	1	0.8426	0.0034	−157.4	3.4	1375	35	800	400	531	605		568	508	632		570	**569**	**1381**	**63**	**61**
D75-PC43: 6–8 cm	Sg1	150,466	P	45.96077	−130.01355	1538	−1	0.8893	0.0031	−117.1	3.1	945	30	800	400	140	242		191	72	269		171	**184**	**1766**	**85**	**112**
D75-PC43: 14–16 cm	Sg1	150,467	P	45.96077	−130.01355	1538	−1	0.8479	0.0031	−158.3	3.1	1325	30	800	400	497	547		522	482	604		543	**527**	**1423**	**77**	**45**
D75-PC43: 23–24 cm	Sg1	147,454	P	45.96077	−130.01355	1538	1	0.8205	0.0030	−179.5	3.0	1590	30	800	400	687	758		723	660	803		732	**727**	**1223**	**76**	**67**
D75-PC43: 23–24 cm	Sg1	147,455	B	45.96077	−130.01355	1538	−1	0.6984	0.0027	−301.6	2.7	2885	35	2060	1660	712	805		759	682	871		777	**764**	**1186**	**107**	**82**
D75-PC58: 21–22 cm	Si1	147,456	P	45.95880	−130.01589	1543	1	0.8220	0.0028	−178.0	2.8	1575	30	800	400	675	741		708	656	783		720	**714**	**1236**	**69**	**58**
D75-PC69: 9–10 cm	Ne	147,457	P	45.96224	−130.01376	1547	1	0.8757	0.0036	−124.3	3.6	1065	35	800	400	268	337	0.870	303	253	412		333	**314**	**1636**	**98**	**61**
																341	357	0.130	349								
D262-PC3: 6 cm	Nj	154,648	P	45.96254	−129.99192	1516	1	0.8848	0.0035	−115.2	3.5	985	35	800	400	147	163	0.132	155	117	300		209	**222**	**1728**	**78**	**105**
																190	215	0.203	203								
																220	277	0.665	249								
D262-PC41: 6.5 cm	Nj	154,649	P	45.96312	−129.99187	1516	1	0.8551	0.0032	−144.9	3.2	1260	35	800	400	461	511		486	428	535		482	**486**	**1464**	**49**	**58**
D262-PC53: 12 cm	Nj	154,651	P	45.96243	−129.99177	1516	1	0.8261	0.0034	−173.9	3.4	1535	35	800	400	653	713		683	630	758		694	**686**	**1264**	**72**	**56**
D270-PC50: <3 cm	Sc1?	154,652	P	45.94880	−129.98501	1469	1	1.0107	0.0036	10.7	3.6	modern		800	400					Modern							
Axial Summit-Caldera Rim																											
D79-PC70: 21–22 cm[a]	Ej4	147,469	P	45.95543	−129.98337	1504	1	0.4495	0.0020	−550.5	2.0	6425	40	800	400	6387	6491		6439	6323	6553		6438	**6440**		**117**	**113**
D79-PC76: 6–7 cm	Ed	147,470	P	45.94970	−129.97589	1523	1	0.8450	0.0035	−155.0	3.5	1355	35	800	400	512	569	0.819	541	497	623		560	**552**	**1398**	**71**	**55**
																578	596	0.181	587								
D79-PC79: 22–23 cm	Eh	147,471	P	45.94773	−129.97678	1510	1	0.7435	0.0031	−256.5	3.1	2380	35	800	400	1491	1595		1543	1416	1648		1532	**1539**	**411**	**109**	**123**
D256-PC59L: 43 cm[a]	We5	154,643	P	45.93445	−130.01913	1410	1	0.2306	0.0010	−769.4	1.0	11,785	40	800	400	12,739	12,922		12,831	12,669	12,983	0.948	12,826	**12,838**		**169**	**145**
																				13,011	13,065	0.052	13,038				
D256-PC77L: 39 cm[a]	We5	159,655	P	45.93453	−130.01836	1415	0	0.0316	0.0006	−968.4	0.6	27,760	170	800	400	31,064	31,255		31,160	30,959	31,354		31,157	**31,160**		**201**	**194**
D259-PC2: 15–16 cm	Wd	154,644	P	45.96513	−130.05379	1457	1	0.7802	0.0027	−219.8	2.7	1995	30	800	400	1119	1215		1167	1065	1242		1154	**1161**	**789**	**81**	**96**
D259-PC6: 16–18 cm	Wd	154,706	B	45.95611	−130.05665	1500	1	0.6681	0.0032	−331.9	3.2	3240	40	2060	1660	1078	1190	0.980	1134	1041	1248	0.980	1145	**1141**	**809**	**107**	**100**
																1193	1197	0.020	1195								
D259-PC65: 3–5 cm	Wc	154,707	B	45.95278	−130.05453	1473	1	0.6846	0.0023	−315.4	2.3	3045	30	2060	1660	898	962		930	857	1030		944	**932**	**1018**	**98**	**75**
D259-PC70: 20–22 cm	Wc	154,708	B	45.95264	−130.05125	1473	1	0.6813	0.0024	−318.7	2.4	3080	30	2060	1660	921	996		959	903	1046		975	**964**	**986**	**82**	**61**
D259-PC46L: 53–55 cm[a]		154,645	P	45.96608	−130.05585	1469	1	0.1766	0.0010	−823.4	1.0	13,930	45	1100	700	15,062	15,275	0.632	15,169	14,934	15,667	0.986	15,301	**15,262**		**328**	**405**
																15,313	15,482	0.368	15,398	15,763	15,834	0.014	15,799				
D259-PC51L: 62 cm[a]		154,646	P	45.96619	−130.05575	1469	1	0.1140	0.0008	−886.0	0.8	17,440	60	1100	700	19,421	19,540		19,481	19,319	19,328	0.002	19,324	**19,483**		**108**	**113**
																				19,375	19,596	0.912	19,486				
																				19,704	19,834	0.086	19,769				
D259-PC51L: 62 cm, duplicate[a]		154,702	P	45.96619	−130.05575	1469	1	0.1166	0.0013	−883.4	1.3	17,260	90	1100	700	18,985	19,085	0.240	19,035	18,918	19,460		19,189	**19,289**		**371**	**171**
																19,252	19,443	0.760	19,348								
D259-PC59L: 45 cm[a]		154,647	P	45.96281	−130.05522	1483	1	0.1689	0.0009	−831.1	0.9	14,290	45	1100	700	15,673	15,729	0.063	15,701	15,393	16,611		16,002	**16,081**		**688**	**530**
																15,862	16,462	0.937	16,162								
D262-PC45L: 17–18.5 cm[a]	Ei2	159,663	B+P	45.96479	−129.99115	1485	0	0.7481	0.0031	−251.9	3.1	2330	35	1430	1030	717	816		767	686	875		781	**770**	**1180**	**105**	**84**
D262-PC52L: 43 cm[a]	Ei2	154,650	P	45.96704	−129.99122	1480	1	0.8067	0.0036	−193.3	3.6	1725	40	800	400	819	917		868	763	953		858	**866**	**1084**	**87**	**103**
D262-PC65, 17–19 cm[a]	Ei2	154,709	B	45.96489	−129.99132	1485	1	0.7136	0.0026	−286.4	2.6	2710	30	2060	1660	569	576	0.056	573	548	669		609	**623**	**1327**	**46**	**75**
																597	657	0.944	627								
D262-PC77, 11–13 cm[a]	Eg	154,710	P	45.96868	−129.99040	1487	1	0.8259	0.0032	−174.1	3.2	1535	35	800	400	653	713		683	630	758		694	**686**	**1264**	**72**	**56**
D270-PC70: 9–11 cm, of 18 cm[a]	Ej5	154,699	B	45.94979	−129.98358	1511	1	0.6743	0.0024	−325.7	2.4	3165	30	2060	1660	1001	1104		1053	962	1148		1055	**1055**	**895**	**93**	**93**

[a]Core did not collect sediment/lava interface. CAMS: Lawrence Livermore National Lab analysis ID; Type: P = Planktic foraminifera, B = Benthic foraminifera. Reservoir correction and Marine ΔR-Factor explained in the text. Median probability (cal yr BP) in calibrated years before present (1950). Median probability (CE) in calendar years. Columns in bold are dates and errors cited in text.

Geochemistry Geophysics Geosystems G3
CLAGUE ET AL.: GEOLOGIC HISTORY OF AXIAL SEAMOUNT
10.1002/ggge.20240

4. Results: Structure

[20] The gross structure of the summit has been known for many years [*Zonenshain et al*., 1989; *Embley et al*., 1990; *Johnson and Embley*, 1990], but the AUV bathymetry adds rich detail. The distribution and orientation of small fissures, cracks, and faults (commonly extracted from side scan data) have been identified entirely from the high-resolution bathymetric data (Figure 2). These faults and fissures define the loci of eruptive activity and the width of the two active rift zones. For example, the eruptive fissures for many of the flows to be described in later sections can be identified in the high-resolution data.

4.1. Caldera

[21] The most striking structural feature of Axial Seamount is the 3.3 by 8.6 km caldera at the summit (Figure 1). The NE part of the caldera floor reaches depths of 1583 m and the floor generally slopes up toward the SSE where the S rim is buried by postcaldera lava flows erupted on the uppermost S rift zone where it extends into the SE part of the caldera (Figure 3). This sloping floor results in general northwestward flow paths for all but one small flow, described below. The shallowest portions of the rim are 1367 m depth to the SE and 1461 m to the NE. The height of the caldera wall is greatest at ~160 m in the W central part of the caldera where a combination of greatest depth of the caldera floor is juxtaposed against the shallowest rim. Figure 3 shows a series of cross sections across the upper rift zones and caldera. For most of the caldera wall, the boundary appears in the mapping data as a single fault with a narrow talus ramp at the base. However, dive observations show a series of near-vertical outcrops of truncated flows offset by talus ramps such that a traverse up the wall from the caldera floor switches back and forth multiple times from near-vertical outcrop to talus. This alternating near-vertical outcrop and talus ramp creates a stairstep pattern that is similar to the observed interior walls in Halema'uma'u crater in Kilauea's summit caldera [*Macdonald*, 1965]. The base of the wall can consist of either a talus ramp or a near-vertical outcrop of truncated flows where subsequent flows on the floor lap against the wall and have buried presumed talus, but the upper wall is near-vertical truncated flows, commonly draped by clastic deposits. In the NW portion of the caldera, the caldera wall is more complex and includes a 1.8 km long section with two arcuate slivers that have slumped downward ~14 and ~7 m (Figure 4a). The faults bounding these slivers transition to fissures with minimal vertical offsets N and S of the down-dropped section.

4.2. Rift Zones

[22] The N rift zone extends NNE at 020°, intersects the caldera near the center of the N rim, and extends into the caldera floor (Figure 5) at the CASM (Canadian_American Seamount (Expedition)) hydrothermal field [*Chase et al*., 1985; *Embley et al*., 1990] where chimneys are located near a fissure that is up to 28 m wide and up to 16 m deep. Despite the width and depth of the CASM fissure, there are no traces of it more than 350 m S of the caldera wall (Figure 2). To the N of the caldera wall, numerous discontinuous, narrow extensional fissures trending 005° in a zone nearly 300 m wide define the N rift zone and cut a pillow ridge (*Flow Wf2 on* Figure 5) aligned with the CASM fissure. A few, possibly eruptive, fissures also occur about 1 km E of the main fissure zone where they are oriented about 010° near the W edge of another volcanic ridge. A few other wider 350-000° fissures are located about the same distance W of the main fissure zone.

[23] The S rift zone also is oriented at about 020° and intersects the SE caldera wall. The upper S rift zone is largely defined by open fissures that fed part of the 2011 flows [*Caress et al*., 2012a] and an earlier flow *(Flow Sa* on Figure 6). Numerous other eruptive fissures roughly coincide with the inferred location of the buried S and SE caldera wall (drawn approximately on Figure 2). Fissures down the S rift near the 1998G–K rift flows [*Chadwick et al*., 2013] crosscut a zone just less than 1 km wide and are offset SE of the *Flow Sa* fissure (see Figures 2 and 6).

4.3. Other Fissures and Faults on Caldera Floor

[24] Open fissures are rare on the caldera floor and are largely limited to the N and W-central caldera floor where they are aligned with the N rift zone (Figure 2). These fissures are commonly the eruptive fissures for the flows that surround them, and collapsed lava ponds and channel systems emanate from them. A fault oriented 070° (labeled Fault A on Figure 2) and with the SSE side dropped down occurs just S of the only cone on the caldera floor, located in the NW portion of the caldera. This is the only fault or fissure with an orientation dissimilar to the rift zones or caldera walls. It may mark the west-northwest rim of a crater within the caldera that is largely filled by later lava flows.

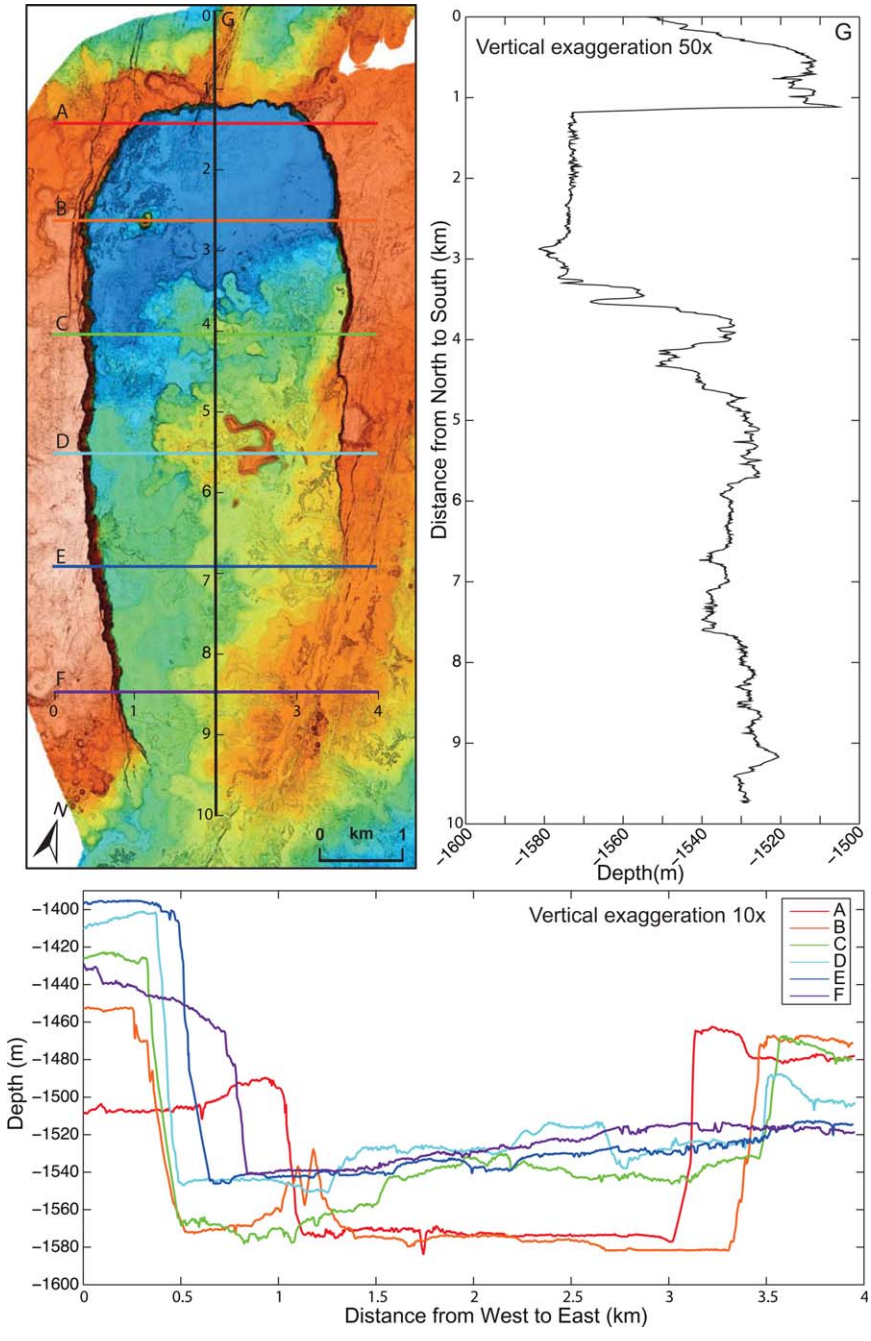

Figure 3. Profiles illustrating the variable depths of the caldera rims and floor. The map has been rotated 17° clockwise and profile G along the long axis is shown to the right. The north caldera floor is nearly flat and then irregularly rises to the south. Cross sections A–F are profiles across the short axis of the elongate caldera and are stacked in a single illustration, centered on profile G. Profiles E, F, and G illustrate that the SE and S caldera walls are buried beneath young flows. Color ramp as in Figure 1.

4.4. Fissures and Faults on Flanks Outside the Caldera

[25] Fissures are common on the E and W flanks (Figure 2). Two types are present: (1) common ones that roughly align with the rift zones and (2) rare ring faults on the rims. Faults on the W flank align roughly with the N rift zone. Faults on the SE and E flank align with the S rift zone, curving to become parallel with the N rift zone to the E of the caldera. The many fissures that align with the rift zones appear to be either spreading or extensional fractures, where they crosscut flow channel

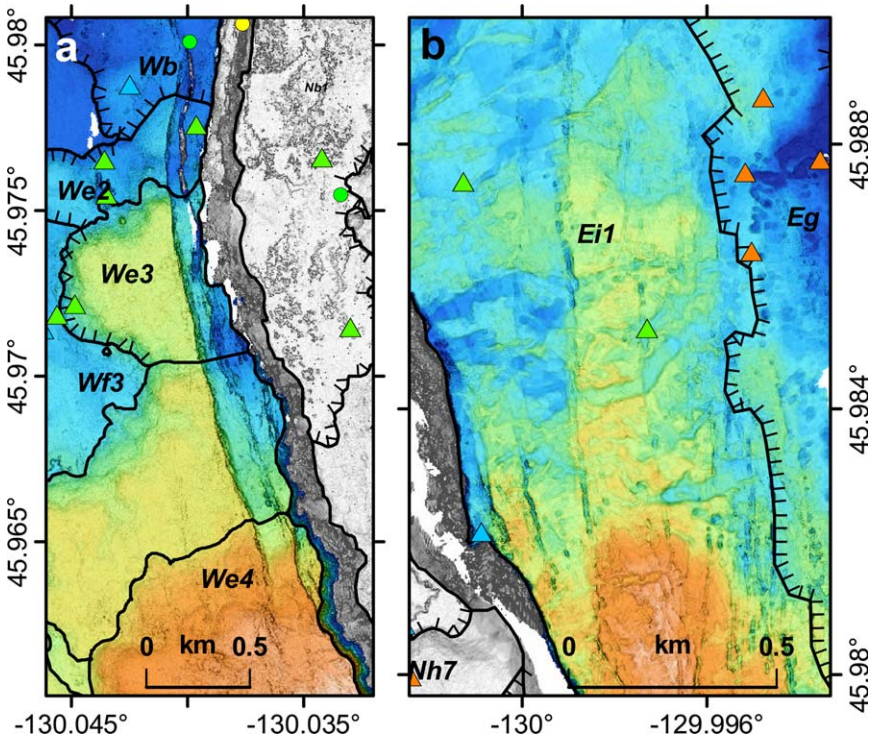

Figure 4. Vertical displacement on caldera rims. Hatchures are on the young side of the flow contacts. Flows are labeled as discussed in the text in this and all subsequent figures; only flows that have been sampled or are distinctive in the side scan data have been assigned flow unit labels. (a) Close-up view of slump blocks on northwest caldera wall. Two blocks are dropped downward into the caldera by ~7 and ~14 m and appear to be rotated with their north ends slumped more than their southern ends. Color ramp is −1496 m (blue) to −1416 m (orange). The gray area to the east is the −1570 m deep caldera floor and is too deep to be included in the 80 m color ramp used. (b) Close-up view of a small area on the east rim of the caldera showing vertical displacements along the fissures, creating a subtle horst-graben terrain. The gray area in the SW corner is the caldera floor. Channels in *flow Ei1* originate to the west at the caldera boundary and flow east-northeast indicating emplacement prior to caldera formation. *Flow Eg* erupted ~1260 CE from fissures on the east rim of the caldera. Most of the *Eg* fissures are filled by late lavas during the eruption, but a string of small depressions near the SE corner of the map mark the fissure. Color ramp is −1476 m (blue) to −1461 m (orange), with the gray areas deeper than the 15 m color ramp.

systems, or eruptive fissures that fed flows. Some have vertical offsets of several meters as well as horizontal displacements, creating subtle horst/graben terrain, especially on the E flank (Figure 4b). Rare circumferential faults around the caldera bound blocks that have subsided adjacent to the caldera (see section 4.1., Figure 4a), and are most prominent on the NW and SW sectors of the caldera.

5. Results: Hydrothermal Vent Fields

[26] The AUV mapped all the known hydrothermal vent fields. The International District, ASHES (Axial Seamount Hydrothermal Emissions Study), and CASM vent fields [*Chase et al.*, 1985; *Embley et al.*, 1990; *Butterfield et al.*, 2004] are illustrated in supporting information Figure S4. The International District, and to a lesser degree ASHES, contains chimneys large enough to be readily detected in the 1 m resolution bathymetry. The AUV data revealed several previously unknown chimneys, including El Guapo in the International District, that were then confirmed as active during subsequent ROV dives in 2006. The hydrothermal vents are included here mainly because we can now identify the flows underlying them and infer their ages and a probable maximum time these vent fields could have been active.

6. Results: Lava Flows

[27] The high-resolution AUV maps reveal the progression of lava flow morphologies within flow

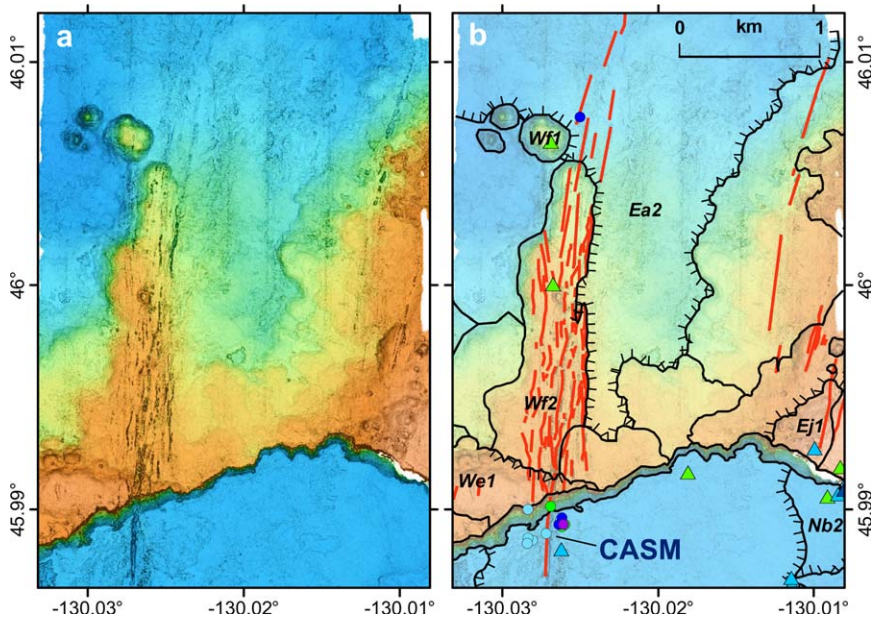

Figure 5. Close-up view of AUV bathymetry of the north rift zone. Only flows that have been sampled or are distinctive in the side scan data have been assigned flow unit identity. Color ramp is −1595 m (blue) to −1505m (orange). (a) The data alone and (b) flow contacts, flow labels as described in the text, hatchures on the young side of contacts, locations of lava samples (colored triangles and dots) coded by MgO content of the glass (as in Figure 1c), radiocarbon-dated cores (colored squares) coded by age (as in Figure 1d), and fissures (from Figure 2, but in red) superposed on faded version of the bathymetry. The same (Figure 5a) bathymetric data and (Figure 5b) interpreted images will be used for most of the detailed maps as well as the line and point symbology.

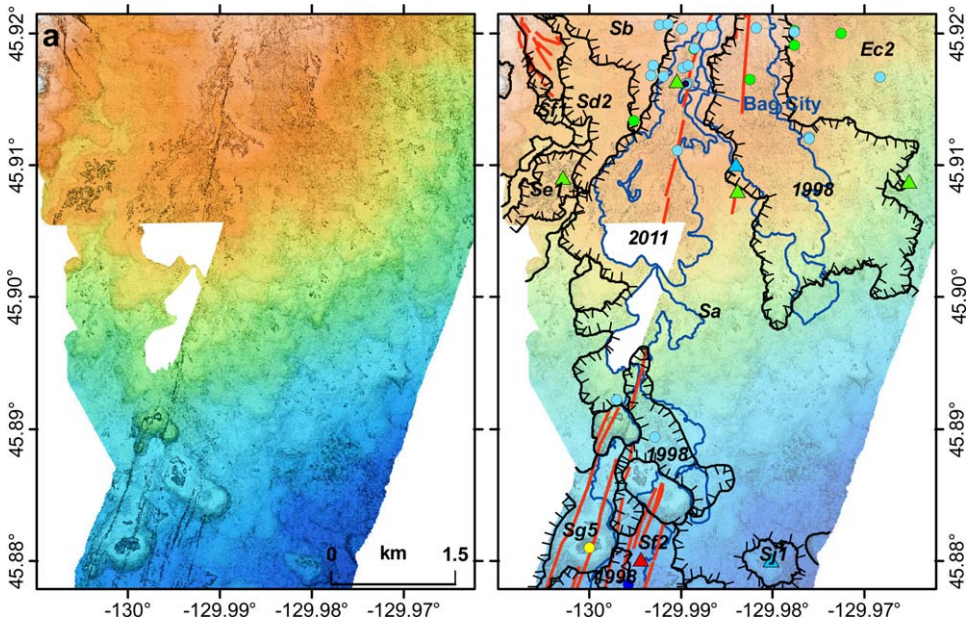

Figure 6. Close-up view of AUV bathymetry of the upper south rift zone. The white region labeled 2011 is an area not surveyed prior to the 2011 eruption that was covered by 2011 lava so is unavailable for this analysis. The area to the SW of that region of the 2011 flow was combined with the pre-2011 surveys to expand coverage. Histogram-equalized color ramp is −1806 m (blue) to −1504 m (orange).

units from the eruptive fissures and flow channels to the pillowed margins. Recognition of the architecture of the flows defines the flow boundaries and also reveals the relative stratigraphic relations where younger flows have buried the channel systems of older flows or ponded against older features. Many flow boundaries identified from the mapping data were also observed and confirmed during subsequent ROV dives or by reviewing video from earlier ROV dives. Numerous prehistoric lava flows within the caldera have sediment cover too thin to collect with cores (<~5 cm), and we infer that they erupted more recently than 1650 CE based on the youngest calibrated radiocarbon ages from cores. Finally, the MgO content of glass rinds on lava samples and relative crystal contents helped distinguish between flows. We have used flow morphology nomenclature as in *Chadwick et al*. [2013].

[28] The stratigraphically youngest prehistoric flows are labeled with "a" following a regional designation (N, S, E, and W, explained below), and increasingly older flows are labeled b, c, d, etc. Thus the stratigraphically youngest flow in the north caldera (the flow underlying the CASM hydrothermal field) is identified as *Flow Na*. In some cases, a single flow is predated by several other flows with unknown stratigraphic relation to one another because they share no contact; they are given designations like *Flow Nb1* and *Flow Nb2* if they appear to be of similar age. The 1998 lava flows are labeled with their year of eruption and the flows from different eruptive fissures are designated as 1998A–K [*Chadwick et al*., 2013]. To make the map units more manageable, we divided the mapped area into four regions with regions north (N) and south (S) mainly within the caldera and separated from one another by a key dated flow (*Flow Ne*). The other two regions are the east (E) and west (W) rims of the caldera and their flow sequences are not directly tied to the first two regions, either due to separation by the caldera wall, or separation by the two historical flows. Figure 7 shows a summary of the flow units, subdivided and separately colored by relative ages for each of the four regions with the youngest flow in each region in red and older flows in increasingly cooler colors. We emphasize that the relative ages of the flow units are based almost entirely on relative stratigraphic positions rather than on the radiocarbon ages.

[29] Table 2 presents the glass chemistry for each flow unit organized by region (including average, range, and standard deviation for MgO and the average concentration for the remaining elements on a volatile-free normalized basis) and crystal content as aphyric (<1% crystals), sparsely plagioclase phyric (3–5%), or plagioclase phyric (>10%) based on data for each sample (supporting information Tables S1 and S2). The compositions of the flows fall into two types. Type 1 lava is consistently aphyric, slightly less depleted (higher K_2O/TiO_2, for example), and has more fractionated glass with MgO <7.9 wt%. Type 2 lava is more depleted (lower K_2O/TiO_2) and has more primitive glass with MgO >7.9 wt%. Type 2 includes all the plagioclase phyric lavas, although not all Type 2 lavas are phyric (see Table 2 and flow descriptions). The two groups are classified as Type 1 and 2 in supporting information Table S1 and the origin of their differences is the central topic of a companion paper by *Dreyer et al*. [2013].

[30] Four flows are listed as both plagioclase phyric and aphyric, as samples of both types are present in what we have mapped as single flows. A flow on the east flank, designated *Flow Eg* is an example, with eight of nine samples plagioclase phyric, but one sample, with similar sediment cover and glass chemistry, is aphyric. As this is the only young flow on the east flank, these samples must all be part of the same flow, despite their varied mineralogy. This result demonstrates that crystal content in generally phyric lava flows can be highly variable due to either eruption dynamics or flow segregation. The phenocryst content of the flows is included in section headings where possible. All younger and older flows that are in contact with each flow unit are indicated in Table 2; those relations will be described in the text for only a few flows that are key to establishing the stratigraphy.

[31] The ages of some of the oldest flows, from the W caldera rim, are constrained by ages of cores collected in 1 m tubes of the thick clastic section on the caldera rim. None of the recovered cores is as long as the core tube penetration as discussed in supporting information 2.3, so all yielded minimum ages, perhaps by substantial amounts. The flows are lobate sheet flows with complex channel systems, and are directed outward from the summit from fissure systems that are missing and whose upstream channel ends are truncated by the caldera wall. We have sketched in some potential flow contacts on the rim (Figures 7c and 7d), but these are poorly constrained due to a paucity of lava samples and because the bathymetry is smoothed and subdued by the overlying 1–2 m thick clastic section.

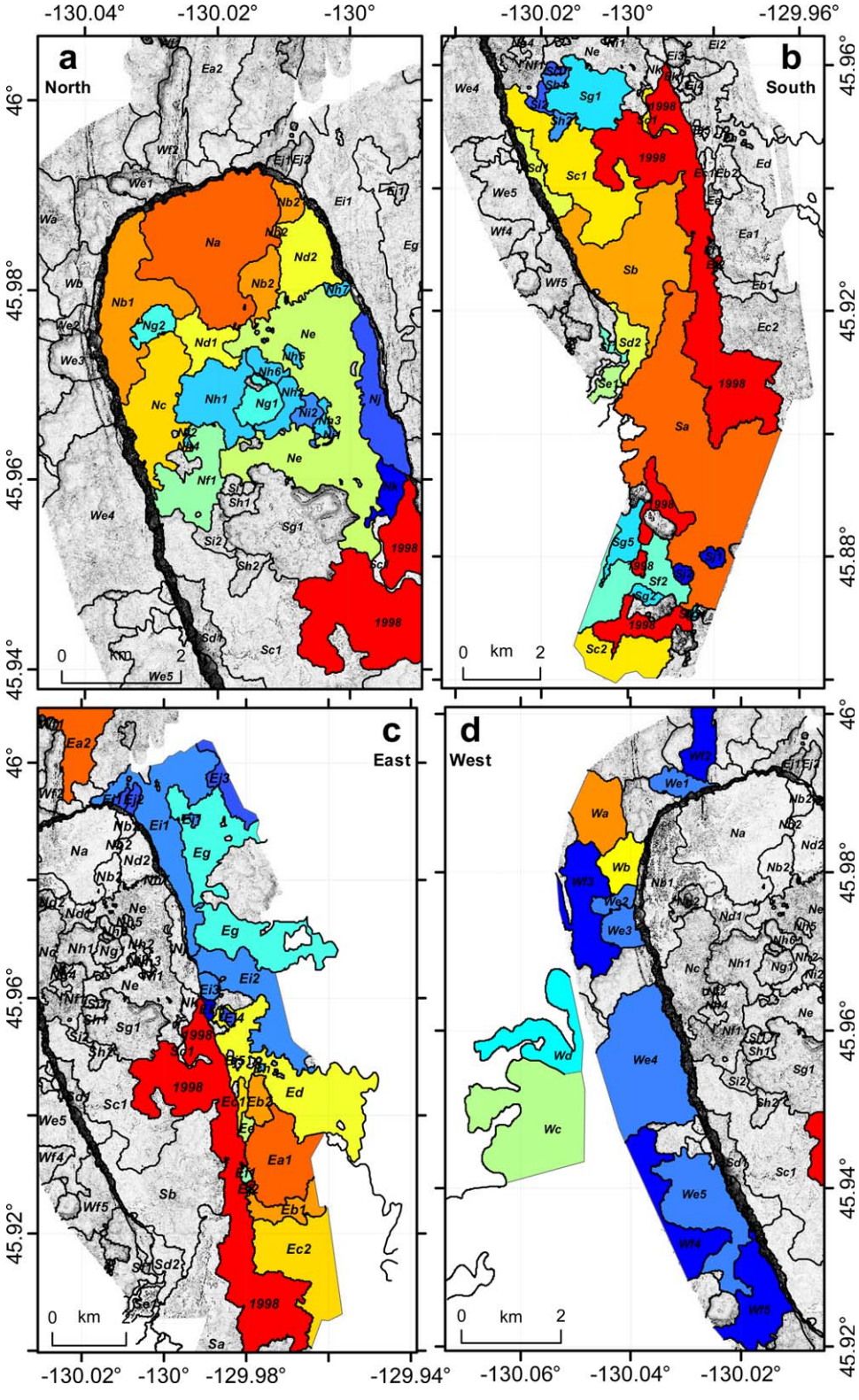

Figure 7. Maps of the four regions discussed in the text showing the relative ages of flows in each area with youngest in red and oldest in dark blue. Flow units are labeled according to relative age and spatial identity as discussed in the text. The four regions are (a) N: the north caldera; (b) S: the south caldera and upper south rift; (c) E: the east caldera rim; and (d) W: the west caldera rim.

Table 2. Average Glass Compositions of Each Flow Unit, Analyses on Normalized Volatile-Free Basis[a]

Flow Unit	Avg #	Crystals	Type	Contacts-Younger	Contacts-Older	SiO_2	TiO_2	Al_2O_3	FeO	MnO	MgO	Min MgO	Max MgO	1σ MgO	CaO	Na_2O	K_2O	P_2O_5
Region North																		
Na (CASM)	37	A	1	None	Nb1, Nb2, Nd1, Nd2	49.96	1.51	14.63	10.91	0.20	7.41	6.71	7.58	0.17	12.15	2.90	0.18	0.15
Nb1	6	A	1	Na	Nc, Nd1, Ng2	49.80	1.52	14.67	10.87	0.20	7.54	7.48	7.62	0.05	12.37	2.74	0.17	0.14
Nb2	3	A	1	Na	Nd2, Ne	49.94	1.55	14.68	10.91	0.20	7.33	7.26	7.54	0.20	12.36	2.71	0.17	0.14
Nc	4	A	1	Nb1	Nd1, Ng2, Nh1	49.86	1.52	14.68	10.89	0.19	7.52	7.44	7.55	0.05	12.31	2.72	0.17	0.15
Nd1	1	A	1	Na, Nb1, Nc	Ne, Nh1	50.18	1.52	14.78	10.78	0.17	7.45				12.20	2.64	0.17	0.12
Nd2	1	A	1	Na, Nb1	Ne, Nh7	49.95	1.44	14.76	11.00	0.19	7.30				12.39	2.66	0.17	0.13
Ne	11	A	1	2011, 1998, Nb2, Nd1, Nd2, Sc1	Nf1, Nh1, Nh2, Nh3, Nh5, Nh6, Nh7, Ni1, Ni2, Nj, Nk, Sg1, Si1	49.54	1.47	15.21	10.35	0.19	7.82	7.64	7.92	0.10	12.38	2.72	0.17	0.14
Nf1	4	A	1	Sc1, Nc, Ne	Nf2, Nh1, Nh4, Sh1, Si1, Si2	49.60	1.51	14.69	10.95	0.19	7.57	7.55	7.60	0.02	12.44	2.73	0.17	0.15
Nf2	1	A	1	Nc, Nf1	Nh4	49.48	1.45	15.12	10.55	0.18	7.84				12.43	2.68	0.14	0.13
Ng1	3	P	2	None	Nh1, Nh2, Nh6	49.22	1.34	15.74	10.13	0.18	8.09	8.00	8.22	0.11	12.41	2.64	0.11	0.12
Ng2	3	P	2	Nb1, Nc, Nd1	None	49.09	1.23	16.39	9.63	0.17	8.58	8.56	8.60	0.02	12.21	2.47	0.12	0.10
Nh1	2	P/A	2	Nc, Nd1, Ne, Nf1	Ng1, Nh6?	48.91	1.28	16.00	10.02	0.18	8.43	8.36	8.50	0.10	12.35	2.60	0.11	0.12
Nh2	1	P	2	Ne, Ng1	Ni2, Nh6	48.79	1.27	16.06	10.00	0.18	8.48				12.41	2.58	0.11	0.12
Nh3	2	P/A	2	Ne	Ni1, Ni2	48.85	1.32	16.09	9.97	0.19	8.46	8.22	8.70	0.34	12.31	2.58	0.12	0.12
Nh4	1	P	2	Nc, Nf1, Nf2	None	48.70	1.28	16.17	9.99	0.18	8.49				12.37	2.61	0.11	0.10
Nh5	1	SP	2	Ne	None	48.88	1.30	16.16	9.84	0.16	8.43				12.33	2.66	0.12	0.10
Nh6	1	P	2	Ne, Nh2	Ng1, Nh1?	49.29	1.33	15.64	10.22	0.17	8.15				12.28	2.66	0.14	0.12
Nh7	2	A	2	Nd2, Ne	None	49.13	1.32	16.27	9.90	0.17	8.27	8.24	8.29	0.04	12.18	2.55	0.13	0.11
Ni1	1	P	2	Ne, Nh3	None	49.16	1.32	15.71	10.11	0.16	8.27				12.40	2.65	0.11	0.12
Ni2	1	P	2	Ne, Nh2, Nh3	None	49.19	1.33	15.81	10.08	0.18	8.14				12.37	2.66	0.12	0.11
Nj	4	SP	2	1998, Ne	Nk	48.70	1.28	16.41	9.78	0.17	8.63	8.49	8.72	0.11	12.22	2.61	0.13	0.11
Nk	7	P	2	1998, Ne, Sc1, Nj	None	48.90	1.31	16.08	9.97	0.17	8.42	8.33	8.61	0.10	12.33	2.58	0.12	0.12
Region South																		
2011	49	A	1	None	Eb1, Ec1, Ec2Ed, Ee, Ej4, Ek1, Ne, 1998, Sa, Sb, Sc1, Sf2, Sg1, Sg2, Sg5	49.83	1.53	14.62	11.05	0.19	7.45	7.25	7.57	0.06	12.27	2.75	0.17	0.14
1998A–F	56	A	1	2011	Sa, Sb, Sc1, Sg1, Ne, Nj, Nk, Ea1, Eb1, Ec1, Ec2, Ee, Ef1, Ef2	50.15	1.53	14.59	10.74	0.20	7.41	7.16	7.72	0.14	12.20	2.86	0.18	0.15
1998G–I	1	A	1	2011	Sa, Sf2, Sg5	50.38	1.53	14.61	10.78	0.20	7.28				12.03	2.89	0.19	0.13
1998J	1	A	1	2011	Sf2, Sg5	50.36	1.58	14.58	10.81	0.21	7.14				12.10	2.90	0.18	0.15
1998K	43	A	1	2011	Sc2, Sf2, Sg2, Sg3, Sg4	49.93	1.55	14.61	11.01	0.19	7.38	6.82	7.66	0.14	12.26	2.75	0.17	0.14
Sa (Bag City)	25	A	1	2011, 1998	Sb, Sd2, Sf2, Sj1, Sj2	50.18	1.52	14.61	10.65	0.20	7.40	7.20	7.60	0.13	12.21	2.89	0.18	0.15
Sb (Ashes)	31	A	1	2011, 1998, Sa	Sc1, Sd1, Sd2	50.20	1.53	14.64	10.66	0.20	7.42	6.94	7.73	0.13	12.12	2.89	0.19	0.15
Sc1	3	A	1	2011, 1998, Sb	Sd1, Sg1, Sh2, Si2, Ne, Nf1, Nk	49.68	1.54	14.74	10.93	0.19	7.48	7.44	7.54	0.06	12.41	2.71	0.17	0.15
Sc2	5	A	1	1998	Sf2	50.37	1.56	14.50	10.85	0.20	7.22	7.16	7.33	0.07	12.05	2.90	0.19	0.15
Sd1	3	A	1	Sb, Sc1	None	49.90	1.52	14.76	10.90	0.20	7.33	7.26	7.45	0.11	12.37	2.70	0.18	0.15
Se1	1	A	1	Sd2	None	49.84	1.52	14.65	10.84	0.19	7.60				12.36	2.69	0.17	0.14

Table 2. (continued)

Flow Unit	Avg #	Crystals	Type	Contacts-Younger	Contacts-Older	SiO_2	TiO_2	Al_2O_3	FeO	MnO	MgO	Min MgO	Max MgO	1σ MgO	CaO	Na_2O	K_2O	P_2O_5
Sf2	2	A	2	2011, 1998, Sa, Sc2	Sg2, Sg5, Sj2	48.67	1.25	16.43	9.88	0.19	8.51	8.43	8.58	0.11	12.32	2.56	0.10	0.11
Sg1	9	A	2	2011, 1998, Sc1, Ne	Sh1, Sh2, Si2	49.00	1.29	15.97	9.93	0.18	8.41	8.21	8.50	0.08	12.36	2.63	0.12	0.11
Sg2	4	A	2	2011, 1998, Sf2	None	49.70	1.35	15.05	10.23	0.19	7.96	7.86	8.05	0.10	12.63	2.65	0.12	0.12
Sg3	1	A	2	1998, Sa	Sg4	49.20	1.39	15.52	10.39	0.18	8.00				12.51	2.58	0.11	0.11
Sg4	1	A	2	1998, Sa, Sg3	None	49.00	1.26	16.06	9.98	0.17	8.30				12.43	2.56	0.10	0.12
Sg5	1	A	2	2011, 1998, Sf2	None	49.64	1.36	15.53	9.99	0.17	8.07				12.15	2.86	0.12	0.12
Sh2	1	P	2	Sc1, Sg1	Si2	48.97	1.30	16.03	9.95	0.18	8.39				12.38	2.58	0.11	0.12
Si1	2	P	2	Ne, Nf1	Sh1	49.04	1.34	15.79	10.18	0.18	8.20	8.18	8.22	0.03	12.41	2.63	0.12	0.12
Si2	1	P	2	Sc1, Nf1, Sg1, Sh1, Sh2	None	49.17	1.34	15.61	10.27	0.19	8.11				12.43	2.64	0.12	0.12
Sj1	1	A	1	Sa	None	49.95	1.59	14.43	11.27	0.20	7.26				12.26	2.73	0.17	0.14
Sj2	1	A	1	Sa, Sf2	None	49.79	1.56	14.51	11.25	0.20	7.30				12.36	2.72	0.17	0.14
Region East																		
Ea1	5	A	1	2011, 1998	Eb1, Eb2, Ed, Ee, Ef1	49.91	1.48	14.79	10.60	0.19	7.64	7.59	7.71	0.05	12.34	2.72	0.18	0.15
Ea2	3		1	None	Wf1, Wf2	50.64	1.50	14.59	10.64	0.20	7.26	7.14	7.46	0.17	11.74	3.04	0.21	0.15
Eb1	3	A	1	2011, 1998, Ea1	Ec2, Ef2	50.05	1.54	14.59	10.76	0.20	7.45	7.37	7.53	0.08	12.28	2.80	0.18	0.14
Ec1	1	A	1	2011, 1998, Eb2	Ed, Ee	49.52	1.52	14.69	10.96	0.19	7.64				12.47	2.70	0.17	0.15
Ec2	9	SP	1	2011, 1998, Eb1	None	49.96	1.49	14.73	10.58	0.21	7.59	7.25	7.79	0.19	12.31	2.82	0.18	0.14
Ed	9	A	1	2011, Ea1, Eb2, Ec1	Eh, Ei2, Ej4, Ej5, Ek1	49.65	1.52	14.72	10.81	0.19	7.62	7.48	7.67	0.06	12.44	2.73	0.17	0.15
Ef1	2	A	2	1998, Ea1	None	49.72	1.25	15.16	10.16	0.18	8.19	8.15	8.22	0.05	12.65	2.49	0.10	0.12
Ef2	2	A	2	1998, Eb1	None	50.15	1.25	15.11	10.09	0.19	8.03	8.02	8.04	0.01	12.35	2.62	0.11	0.11
Eg	9	P/A	2	None	Ei1, Ei2, Ej3	49.27	1.31	15.78	10.03	0.17	8.31	8.17	8.38	0.07	12.29	2.62	0.12	0.10
Eh	2	P/A	1	Ed	None	49.65	1.62	14.16	11.68	0.20	7.35	7.23	7.46	0.16	12.30	2.73	0.16	0.15
Ei1	8	A	1	Eg	Ei2?, Ej2, Ej3	49.83	1.45	14.85	10.76	0.19	7.57	7.48	7.62	0.04	12.42	2.63	0.16	0.13
Ei2	4	A	1	Ed, Eg, Ei3	None	49.71	1.47	14.82	10.79	0.18	7.65	7.53	7.73	0.09	12.44	2.65	0.16	0.14
Ei3	2	A	1	None	Ei2, Ek1	49.76	1.53	14.66	11.09	0.20	7.43	7.27	7.58	0.22	12.34	2.69	0.17	0.14
Ej1	1	A	1	Ej2?	Ej2?	49.93	1.56	14.52	11.10	0.21	7.28				12.36	2.73	0.17	0.15
Ej2	2	A	1	Ei1, Ej1?	Ej1?	49.97	1.52	14.51	11.05	0.20	7.52	7.48	7.55	0.05	12.28	2.66	0.17	0.15
Ej4	1	A	1	2011, Ed	None	49.52	1.50	14.72	11.05	0.19	7.51				12.54	2.65	0.17	0.14
Ej5	2	A	1	Ed	None	49.88	1.43	14.90	10.74	0.19	7.57	7.49	7.65	0.11	12.43	2.60	0.14	0.13
Ek1	1	A	1	Ed, Ei3	None	49.50	1.51	14.81	11.08	0.19	7.53				12.42	2.65	0.17	0.14
Region West																		
Wb	2	A	1	Wa	We2, Wf3	49.73	1.57	14.93	10.81	0.21	7.43	7.32	7.54	0.16	12.13	2.91	0.16	0.16
Wc	6	A	1	None	Wd	49.90	1.54	14.55	11.15	0.19	7.37	7.28	7.53	0.10	12.28	2.72	0.17	0.14
Wd	7	A	1	Wc	None	49.77	1.50	14.66	11.07	0.19	7.39	7.30	7.49	0.08	12.47	2.65	0.16	0.13
We1	1	A	1	None	Wf2	50.31	1.50	14.62	10.57	0.21	7.35				12.18	2.93	0.19	0.14
We2	3	A	1	Wb	We3, Wf3	49.61	1.51	14.92	10.84	0.20	7.58	7.50	7.69	0.10	12.32	2.71	0.15	0.14
We3	1	A	1	We2	Wf3	49.83	1.53	14.65	10.84	0.21	7.56				12.45	2.63	0.17	0.15
We4	2	A	1	None	Wf4	49.59	1.50	14.93	10.95	0.19	7.53	7.49	7.56	0.05	12.40	2.65	0.16	0.13
We5	4	A	1	None	Wf4, Wf5	50.02	1.47	14.82	10.78	0.19	7.47	7.41	7.55	0.06	12.36	2.62	0.16	0.13
Wf1	1	A	1	Ea2	None	49.89	1.55	14.64	10.99	0.18	7.50				12.28	2.67	0.18	0.13
Wf2	1	A	1	We1	None	49.75	1.48	14.83	10.82	0.17	7.69				12.24	2.72	0.17	0.12
Wf3	2	A	1	Wa, Wb, We2, We3	None	49.79	1.47	14.94	10.65	0.19	7.56	7.49	7.62	0.09	12.48	2.62	0.17	0.15
Wf4	1	A	1	We4, We5	None	49.92	1.46	14.65	11.00	0.18	7.56				12.23	2.71	0.17	0.13
Wf5	4	A	1	We5	None	50.34	1.49	14.75	10.62	0.21	7.43	7.31	7.60	0.13	12.01	2.83	0.18	0.15

[a]Flow units defined in text. Avg is the number of analyses averaged. Crystals are A = aphyric or <1%, SP = sparsely plagioclase phyric (3–5%), and P = plagioclase phyric (>10%). Contacts-younger indicates younger flows in contact with the flow unit. Contacts-older indicates older flows in contact with the flow unit. Min MgO indicates minimum MgO of samples averaged, Max MgO indicates maximum MgO averaged, and 1σ MgO indicates the 1σ standard deviation on the average.

Geochemistry Geophysics Geosystems G3

CLAGUE ET AL.: GEOLOGIC HISTORY OF AXIAL SEAMOUNT

10.1002/ggge.20240

[32] Our reconstruction of the summit history is based on the mapping and sampling completed before the 2011 eruption, except for a small area mapped in 2011 but that lies outside the 2011 flows on the upper S rift zone and had not been mapped previously. However, we first describe the inflated lobate flows at the summit and upper S rift that erupted in 2011 and 1998. For reference, the 2011 flow contacts from *Caress et al*. [2012a] and 1998 flow contacts from *Chadwick et al*. [2013] are shown on Figure 1b. Characteristics of these two flows as revealed in the AUV mapping data [*Caress et al*., 2012a; *Chadwick et al*., 2013] are used to interpret contacts and the distribution of lava morphologies in older flows, but they also subdivide regions S from E. We then describe the flows in the N, S, E, and finally W regions starting with the youngest flows and ending with the oldest. Finally, we combine the four regions into a unified geologic history of the summit region. Correlation among the four regions, because the historic flows separate several of the regions, depends heavily on a few key radiocarbon ages.

6.1. Type 1 Historical Inflated Lobate Flows

[33] Historical lava flows were emplaced at Axial Seamount in 1998 [*Embley et al*., 1999; *Chadwick et al*., 2013] and 2011 [*Chadwick et al*., 2012; *Dziak et al*., 2012; *Caress et al*., 2012a]. Mapping prior to the 1998 eruption consisted of shipboard multibeam bathymetry, SeaMarc I side scan, camera tows, and submersible observations [*Zoneshain et al*., 1989; *Embley et al*., 1990]. The 1998 flow was explored extensively soon after its eruption, including mapping with 30 kHz Simrad multibeam bathymetric data [*Embley et al*., 1999], submersible dives, and the 1 m resolution bathymetry collected by AUV presented here. *Chadwick et al*. [2013] describe the 1998 flows and their emplacement in detail. The 2011 flows were discovered several months after their eruption [*Chadwick et al*., 2012] and mapped with the same AUV in August 2011, which enabled a direct comparison of the before and after bathymetry to define the new flows in detail [*Caress et al*., 2012a] and analysis of the architecture of the different lava types within the flows.

6.1.1. Inflated Lobate Flows Erupted in 2011

[34] *Caress et al*. [2012a] described the 2011 lava flows based on 1 m lateral and 20 cm vertical resolution difference maps produced from pre-eruption and posteruption AUV surveys. The outline of these flows is shown on the pre-2011 bathymetry in Figure 1b; the 2011 flows cover many lava flows that were mapped and sampled prior to the eruption and are described here. The 2011 eruption produced five major flows from a series of *en echelon* and discontinuous fissures that extend almost 30 km from the eastern caldera wall down the S rift. The flows in the caldera and on the upper S rift are inflated lobate flows with well-developed dendritic channel systems and inflated pillow flows at their distal ends, but at the S edge of our AUV map coverage, a pillow ridge was produced above the eruptive fissure [*Caress et al*., 2012a]. The 2011 flows in and near the caldera cover 7.8 $\times$ 10^6 m^2, have an average thickness of 3.5 m, and have a volume of 27 $\times$ 10^6 m^3 [*Caress et al*., 2012a].

[35] Several features were revealed in the well-defined 2011 lava flows that can be applied to our analysis of prehistoric flows. These include the reoccupation of fissures from prior eruptions, which resulted in remarkable mimicry by the 2011 flows of the underlying 1998 and earlier flows [*Caress et al*., 2012a]. This characteristic limits our ability to distinguish prehistoric flows that might also have reoccupied pre-existing fissures and flow channel systems, as successive flows may appear to be simply early and late phases of a single eruption. Compound flows are especially common in the southern end of the caldera and uppermost S rift, and some of these may consist of lava flows from more than a single eruption. A second characteristic, also observed on the East Pacific Rise [e.g., *Sinton et al*., 2002; *Soule et al*., 2009; *Fundis et al*., 2010] is that flows graded outward from drained channels of sheet lava to lobate lava and eventually to pillowed margins, and this progression can be used to identify locations of eruptive fissures, constrain flow units, and trace the margins. A third useful feature mapped in the 2011 flows is that some distal pillow flow margins are inflated, often with flow interiors inflated by 5–15 m, and others have collapsed, depending on the original slope of the topography and the sequence of events during an eruption. Finally, the individual flow lobes extend as far as 3.6 km from their eruptive fissures and provide a guideline that individual flows might be multiple kilometers long.

[36] Microprobe glass analyses and other geochemical data of the 2011 flows will be presented elsewhere; the average composition of 49 samples collected during three cruises (by W. Chadwick and D. Butterfield, D. Clague, and J. Delaney and

D. Kelley. This is not a reference to a publication, simply acknowledgement of who collected the samples in 2011.) from 2011 flows in the caldera and upper S rift zone is included in Table 2 and is indistinguishable from the 1998 flows.

6.1.2. Inflated Lobate Flows Erupted in 1998

[37] The 1998 eruption produced four discrete flows [*Chadwick et al*., 2013]. The northernmost and largest by far is a compound inflated lobate flow that erupted from six *en echelon* fissures in and near the caldera (from N to S called A to F by *Chadwick et al*. [2013]). Farther S, three, small, inflated lobate flows erupted from fissures G–I, J, and K near the S extent of our AUV mapping coverage on the upper S rift [*Chadwick et al*., 2013]. All flows erupted through fissures that were largely reoccupied by the 2011 eruption, most of which were also present before the 1998 eruption, as shown by side scan data collected in the 1980s [*Embley et al*., 1990]. The flow erupted from fissures A–F covers 5.8×10^6 m^2, and has a calculated volume of 22×10^6 m^3 [*Chadwick et al*., 2013], for an average flow thickness of 3.8 m.

[38] A characteristic of the flow erupted from the K fissure bears on analysis of mapped prehistoric flows. The flow that advanced down a steep slope to the east-northeast consists of a shingled stack of five flow lobes [*Chadwick et al*., 2013, Figure 20], where each younger lobe advanced a shorter distance from the fissure and partially buried a collapsed and drained core of the prior lobe. Such partial overlaps of collapse features have been used here to identify flow contacts, but such features can clearly be produced during single eruptions, presumably as the eruption wanes, flux decreases, and the flow lobes step back toward the fissure. This observation makes it difficult to distinguish flow lobes from a single eruption from overlapping flows of different ages, even when a contact is observed from the ROV. In either case, the distal flows are older and the proximal ones younger. Barring further evidence, such as different chemistry, sediment cover, or absolute ages, several such potentially compound or shingled flows are interpreted to be flows from single eruptions.

[39] *Chadwick et al*. [2005] present 37 chemical analyses of glass samples from the 1998 flow lobes erupted from fissures A–E in the caldera (note that four *Pisces* submersible samples xl1730-2-3, xl1730-4, xl1730-6-7, and xl1730-MC5 (supporting information Table S2) were collected in 1988 and, therefore, sampled flows buried by the 1998 flow), one analysis of the fissure G–I lava flow, one analysis of the fissure J flow, and six analyses of the fissure K flow. We added 10 samples from the fissure A–E lava flow and 35 more from the fissure K flow. The average compositions for the different 1998 flows are presented in Table 2.

6.2. Prehistoric Lava Flows in Region N

[40] The flows in region N (Figure 7a) include a younger group of Type 1 inflated lobate and sheet flows similar to the historical flows and an older group of Type 2, generally plagioclase-phyric, pillow and inflated lobate flows with glass rinds with higher MgO content. The two groups are separated by inflated lobate *Flow Ne* dated at ~1650 CE. *Flow Ne* is Type 1 lava but has slightly higher MgO than younger Type 1 lavas.

6.2.1. Type 1 Inflated Lobate and Sheet Flows More Recent Than ~1650 CE

[41] *Flow Na* (Figure 8), erupted from a fissure (350 m long, up to 28 m wide, and up to 16 m deep) where the CASM hydrothermal vents (supporting information Figure S4a) are located, is the youngest flow on the northern caldera floor. It is one of only four flows (including the 1998 and 2011 flows) not partly covered by subsequent flows. The flow covers a little less than 2×10^6 m^2, and has an estimated volume of 7×10^6 m^3, if we use an average flow thickness of 3.5 m determined for the 2011 flows [*Caress et al*., 2012a]. The CASM hydrothermal vents and surrounding young lava flow were present in 1983 when first explored [*Chase et al*., 1985; *Embley et al*., 1990]. *Embley et al*. [1990] refer to *Flow Na* as the CASM Flow and mapped smooth-floored lava channels (lineated sheet flows) within the flow and depicted most of the flow as jumbled or hackly sheet flows based on side scan data. We reserve "CASM" to describe the hydrothermal vent site, and refer to the flow as *Flow Na*. The new mapping data demonstrate that it is an inflated lobate flow with well-developed channels and pillowed flow margins. This flow spread out on nearly flat ground (<5 m/1 km) and flowed slightly less than 1.7 km S and 1.2 km E from the source fissure. Numerous 1–2 m tall lava spires were observed in this flow. Several of these lava spires were investigated during *Jason II* dive 290 (supporting information Figure S1) as they superficially resembled small hydrothermal chimneys in the 1 m bathymetric data. These formed as lava crust along channel margins accumulated on obstructions and slowly spun as lava flowed by; they are distinct in form and origin from lava pillars. The flow left a

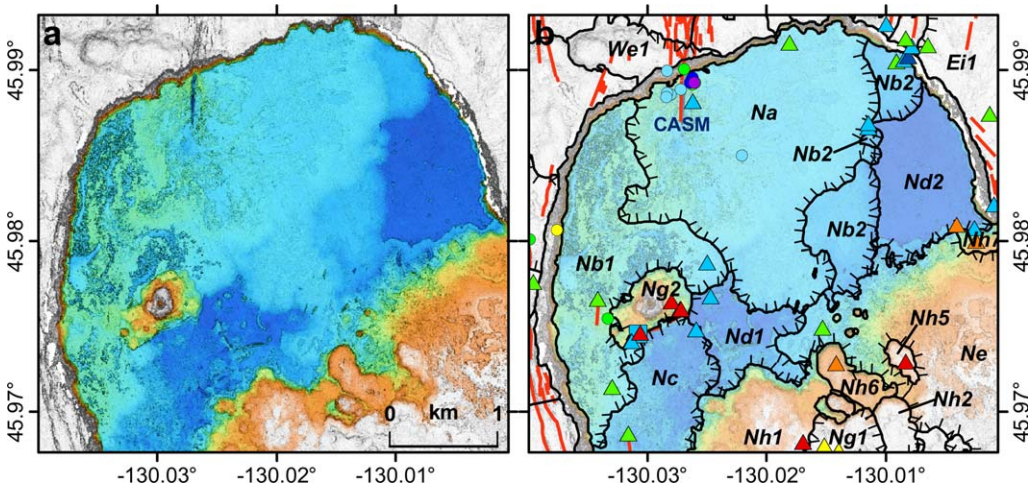

Figure 8. Close-up view of AUV bathymetry of the north caldera showing (a) bathymetry and (b) flow contacts, fissures and fractures, flow unit labels, and glass compositions (also shown on the north and northeast caldera rim). The CASM vent field [*Butterfield et al*., 2004] is labeled. Color ramp is −1585 m (blue) to −1545 m (orange).

narrow 1.5 m high "bathtub ring" of lava around much of the north contact with the base of the talus slope at the foot of the caldera wall. Virtually no blocks have fallen from the wall onto this flow, as is observed around the base of the caldera wall elsewhere.

[42] The next two older lobate *Flows Nb1* and *Nb2* share no contacts (Figure 8), so their relative ages are unknown. Lobate *Flow Nb1* apparently erupted from a 2 km long fissure SW of, and parallel to, the *Flow Na* fissure; the fissure is only visible in the AUV bathymetry for ∼150 m, but the approximately linear channel and pond system suggest it was closer to 2 km long. The flow spread along the W caldera wall, leaving behind a lava bathtub ring at the base of the caldera wall about 3 m above the floors of the drained channels. The shallowest part of the flow is W of an older pillow cone with summit crater, labeled *Flow Ng2*. *Embley et al*. [1990, Figure 7b] include a side scan image showing what they tentatively identified as lava tubes, but these sinuous features are drained lava ponds and channels. Lobate *Flow Nb2* crops out as three remnants E and SE of the CASM hydrothermal field (Figure 8); the flow probably erupted near CASM and is largely covered by *Flow Na*. This flow may be an early, more extensive, phase of the same eruption that produced *Flow Na*.

[43] The next older flow is hackly or jumbled sheet *Flow Nc* that erupted from a fissure that produced a low ridge oriented nearly parallel to the caldera wall at about 345° to the SE of cone *Ng2* (Figure 9). The flow is unusual because the distal flow margins are hackly sheet lava and the fissure is not parallel to the north rift. There is a subtle texture in the distal northern portion of the flow revealed in the AUV data that consisted of 1–2 m tall and several m wide arcuate ridges of the broken surface slabs when observed from the ROV. This is the only flow on ridge axes mapped with the MBARI AUV at Axial or elsewhere [Endeavour Ridge, CoAxial, North Cleft, North Gorda; *Clague et al*., 2010; or Alarcon Rise; *Clague et al*., 2012; *Caress et al*., 2012b] that displays this subtle, 1–2 m amplitude fold-like surface texture in the AUV data.

[44] The next older flows are flat ponded sheet *Flows Nd1* and *Nd2* (Figures 8, 9, 10, and 11). The two flows have distinct glass chemistries that distinguish them from each other, as their morphology and inferred age (based on relative sediment accumulation) are similar. Sheet *Flow Nd1* is located in the north central caldera (Figure 8). Within the flow, a series of raised discontinuous levees up to 14 m tall surround a small central mound that may mark the location of an eruptive vent located east of the trend of the *Na* fissure (Figure 10). The lava pond breached the levees in numerous places and spread out over an unknown area mostly covered by subsequent flows. *Embley et al*. [1990] include side scan imagery of this feature and describe it as a ring structure in their Figure 7b.

[45] Sheet *Flow Nd2* is a remarkable lava pond in the northeast portion of caldera floor (Figures 8 and 11). The pond is surrounded by lava high-stand rims (like a bathtub ring) on its south and east sides. These lava high stands are 4 m above

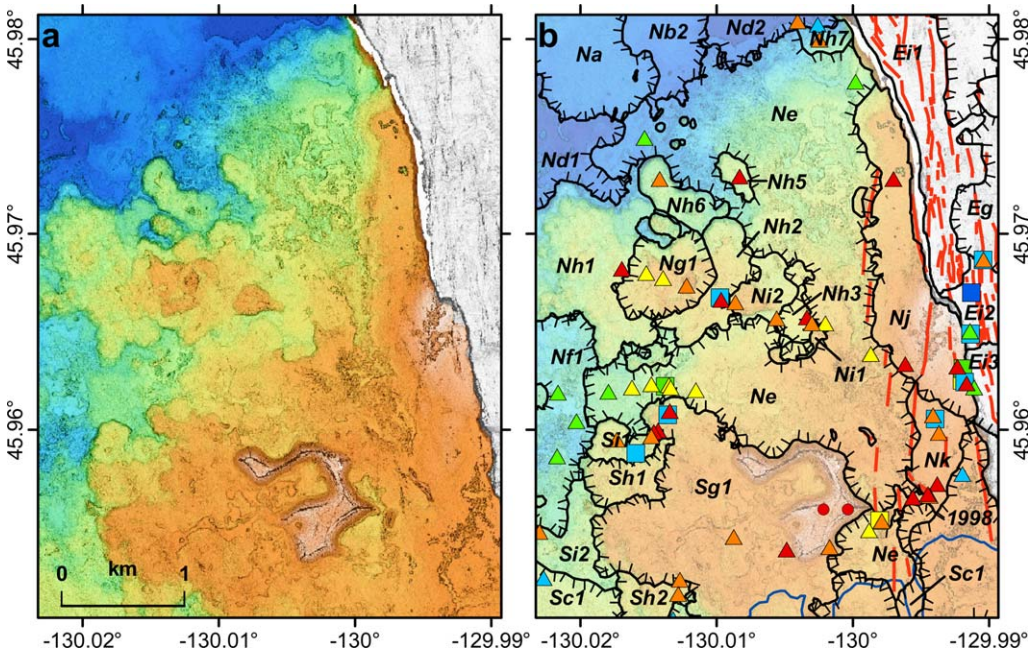

Figure 9. Close-up view of AUV bathymetry highlighting *Flow Ne* in the central caldera. This flow is dated twice at ~1650 CE and grounds much of the stratigraphy presented because of its central location and contacts with so many flows. Color ramp is −1585 m (blue) to −1510 m (orange).

the subsided floor of the pond. The flat pond surface is disrupted at 20 locations by mound-like structures (13 large and 7 small). These features consist of near-vertical slabs of the lake crust up to 1 m thick that buckled upward as the pond surface subsided when the pond drained after cooling long enough for the ~1 m thick crust to solidify. The east margin is ponded against and buries talus at the base of the caldera wall, and was described as a "bench" by *Embley et al.* [1990]. Their side scan image [*Embley et al.*, 1990, Figure 8a] shows some of the mounds that consist of uptilted crust slabs as well. The floor of the lava lake and the high lava mark levees are no longer horizontal (they are just over 1 m deeper on the N than the S end). No eruptive fissure is visible.

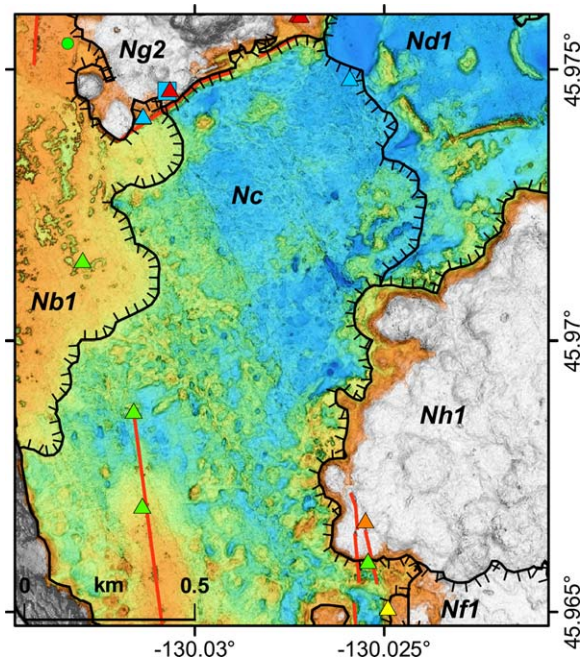

Figure 10. Close-up view of AUV bathymetry of *Flow Nc*, a hackly or jumbled sheet flow in the north caldera. The subtle texture is produced by meter-scale folds in the upper surface of the flow. This is the only flow mapped to date that is jumbled to the flow margins. Color ramp is −1585 m (blue) to −1565 m (orange).

6.2.2. Type 1 Inflated Lobate Flow Ne Erupted in ~1650 CE

[46] Lobate sheet *Flow Ne* (Figures 7a and 9) erupted from a series of seven *en echelon* fissures extending about 2 km across the east central caldera floor. These fissures are oriented parallel to the northern extent of the S rift zone on the E rim of the caldera (Figure 2). One lobe flowed N in braided drained channels and is beneath *Flows Na, Nd1, and Nd2* on the northeastern caldera floor, and a second lobe, also with distinct drained channels, flowed W, dividing older pillow mounds and inflated flows into N and S portions. To the S, the flow underlies *Flow Sc1*, as well as the two historical flows. In the central caldera, *Flow Ne* is dated at ~1650 CE by two cores (1664+117/-58 and 1636+98/-61 CE, Table 1) and is the youngest

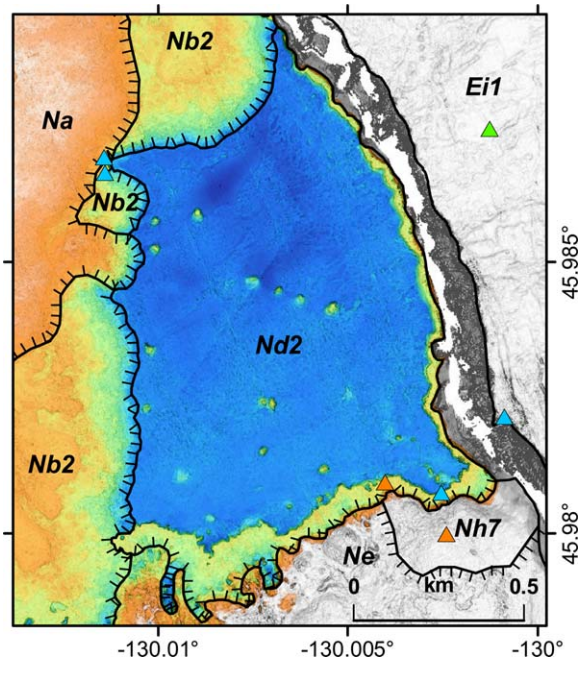

Figure 11. Close-up view of AUV bathymetry of *Flow Nd2*, a ponded lava flow in the northeast caldera. The flow formed a pronounced bathtub ring around the east caldera wall and south sides where it ponded against *Flows Nh7* and *Ne*. The pond is covered by younger *flows Nb2* and *Na* to the northwest. The bright spots in the pond mark places where the 1 m thick crust buckled over underlying high points as the pond subsided when lava drained out. Color ramp is −1583 m (blue) to −1573 m (orange).

radiocarbon-dated flow at Axial Seamount. The flow is a key to understanding the lava flow stratigraphy in the caldera as it is partly covered by younger flows in both the N and S regions.

[47] Glass chemistry of *Flow Ne* lavas decreases in MgO away from the eruptive fissures with near-vent samples (D74-R10, D74-R11, and D74-R21) containing ~7.95 wt% MgO. Distal samples to the W (D75-R7 to R12) are compositionally similar with ~7.95–7.8 wt% MgO, but distal samples of the N lobe (Ax11-RC4 and J2–288-R11) contain ~7.65 wt% MgO (all Type 1; supporting information Table S1). Similar spatial-compositional variations are not observed for other young flows at Axial Volcano, including the extensively sampled historical flows.

[48] *Flows Nf1* and *Nf2* appear to be similar in age to *Flow Ne* based on sediment cover. The roughness of the surfaces of *Flows Nf1, Nf2*, and *Nh4* impeded recovery of cores, despite some sediment present on the flow surfaces. *Flow Nf1* is also more recent than *Flow Si1*, dated at 1236+69/-58 CE. Observations during ROV dive D75 show that *Flow Nf1* consists of topographically rough, complex, drained channels and jumbled sheet flows making it difficult to map its boundaries; it may be more than a single flow. However, the glass is Type 1 and similar to that of nearby lava flows more recent than ~1650 CE and distinct from a group of ~1260–1305 CE Type 2 lavas flows, to be described next.

6.2.3. Type 2 Inflated Lobate and Pillow Flows Erupted ~1264–1305 CE

[49] The N caldera floor has a complex of pillow mounds and inflated flows, a separate cone with summit crater, and scattered remnants of similar flows with plagioclase-phyric glass rinds that have been surrounded and partly buried by younger lobate flows already described (Figures 7a, 8, and 9).

[50] The older lavas are located N and W of *Flow Ne* and consist of at least 12 flows. Inflated *flows Ni1 and Ni2* are similar in structure to the large inflated *Flow Sg1* to the S, but much smaller in area and thickness. *Flow Nh1* consists of overlapping pillow mounds. Inflated flow *Ni1* is largely overrun by *Flow Ne* and only small remnants of the inflated flow remain. This series of flows are plagioclase phyric to ultraphyric lavas (Table 2 and supporting information Table S1). The group of flow units has yielded but a single age for *Flow Nh2* of 1305+67/-91 CE. Two additional cores, collected on *Flows Nh1* and *Ng1* did not yield adequate foraminifera to date but have similar sediment cover and are likely similar in age to *Flow Nh2*. Four other pillow flow remnants with similar compositions and mineralogy are labeled *Nh4 to Nh7*.

[51] A pillow cone *Ng2* with a deep summit crater is located in the NW portion of the caldera floor (Figures 8 and 12a). It is the only cratered cone on the caldera floor or upper flanks of the seamount. *Embley et al.* [1990] called it the Fissure Cone, described it based on side scan data, and descended into the crater during *Alvin* dive 2085. The cone is approximately 45 m tall (measured on the S side) and the summit crater is roughly circular and 70–75 m across and at least 39 m deep from the shallowest part of the rim at 1520 m. Two 5–7 m deep pit craters are located on its E and NE flanks. The S side of the cone and most of the flows are truncated by a normal fault with the S-SE side dropped down (fault A on Figure 12a). A single flow lobe appears to cover this fault. The cone is dated at 1300+57/-60 CE and is constructed of plagioclase-phyric lava.

[52] Sheet *Flow Nj* extends for 2 km along the base of the E caldera wall (Figures 7a and 9). It is

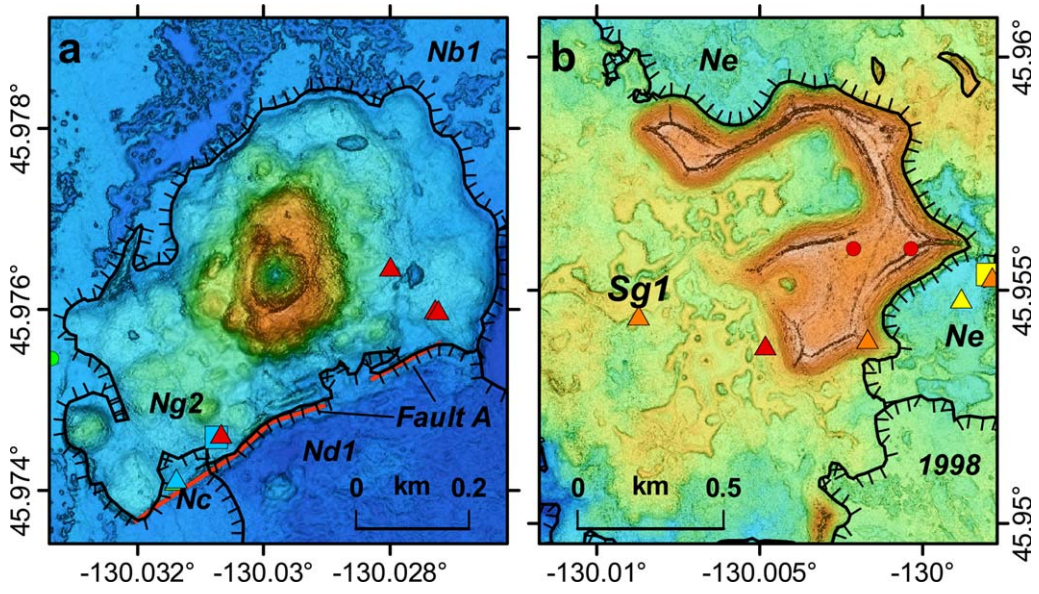

Figure 12. (a). Close-up view of AUV bathymetry of cone *Ng2* on the north caldera floor. The cone has a summit crater and two shallow collapse pits on the east and northeast flanks; fault A forms the southern boundary. The cone formed ~1300 CE. Color ramp is −1585 m (blue) to −1510 m (orange). (b). Close-up view of inflated sheet *flow Sg1* in the central caldera that erupted ~1220 CE. The "Paw Flow" [*Appelgate and Embley*, 1992] just to the west, flowed westward under the label "Sg1." Color ramp is −1550 m (blue) to −1510 m (orange).

unusual in having a series of 11 collapse pits in a sinuous line for the N half of the flow. These may be skylights along a tube system, as described by *Peterson et al*. [1994] on Kilauea and by *Fornari* [1986] on the seafloor, although some are large and deep for skylights. These pits are as much as 13 m deep and the largest is 58 m wide, although most are <15 m across. The S part of the flow has abundant drained lava ponds and channels that emanate from a poorly defined eruptive fissure oriented ~010°. It is these channels and ponds that classify the flow as an inflated lobate flow, despite much of the flow appearing to consist of pillow lava. Three cores were collected for dating because the flow surface was irregular and core recovery was unpredictable. All three cores yielded adequate foraminifera for dating but nonoverlapping ages of 1728+78/-105, 1464+49/-58, and 1264+72/-56 CE with the oldest age from the longest core and the youngest age from the shortest core. The shortest core also lost some basal sediment before it could be stowed in its quiver, thus leading to our decision to collect multiple samples from this flow. The oldest of these three ages is the minimum age of the underlying flow.

[53] Lobate *Flow Nk* is located between *Flow Ne* and the east caldera wall. It consists largely of lobate and pillow textures with a few dendritic collapses, some aligned N-S and apparently marking the location of the eruptive fissure. A single radiocarbon age of 1381+63/-61 CE is slightly too young as the flow is stratigraphically older than *Flow Nj* (Figure 9), dated at 1264+72/-56 CE, but consistent with loss of the basal ~1–1.5 cm of sediment (of about 8 cm total penetration) before the core was stowed in the quiver. *Flows Nj and Nk* differ from others in this age group in being aphyric to sparsely plagioclase phyric.

6.3. Prehistoric Lava Flows in Region S

[54] Region S (Figure 7b), like region N, contains two main groups of lavas: a younger group of Type 1 inflated lobate and sheet flows and an older group of Type 2, generally plagioclase-phyric pillow and inflated lobate flows. Both groups of lavas erupted more recently than 1220 CE.

6.3.1. Type 1 Inflated Lobate Flows More Recent Than ~1650 CE

[55] Inflated lobate *Flow Sa* (Figures 7b and 13) is located S of inflated lobate *Flow Sb* and west of the 1998 and 2011 flows. The flow is now largely buried by the 2011 flows. *Flow Sa* had a very glassy and sediment-free surface in 1998–1999. *Embley et al*. [1990] argued that it was the youngest flow in the caldera (before the 1998 eruption). *Chadwick et al*. [2013] refer to this flow as pre-1982 because it is evident in the 1982 side scan

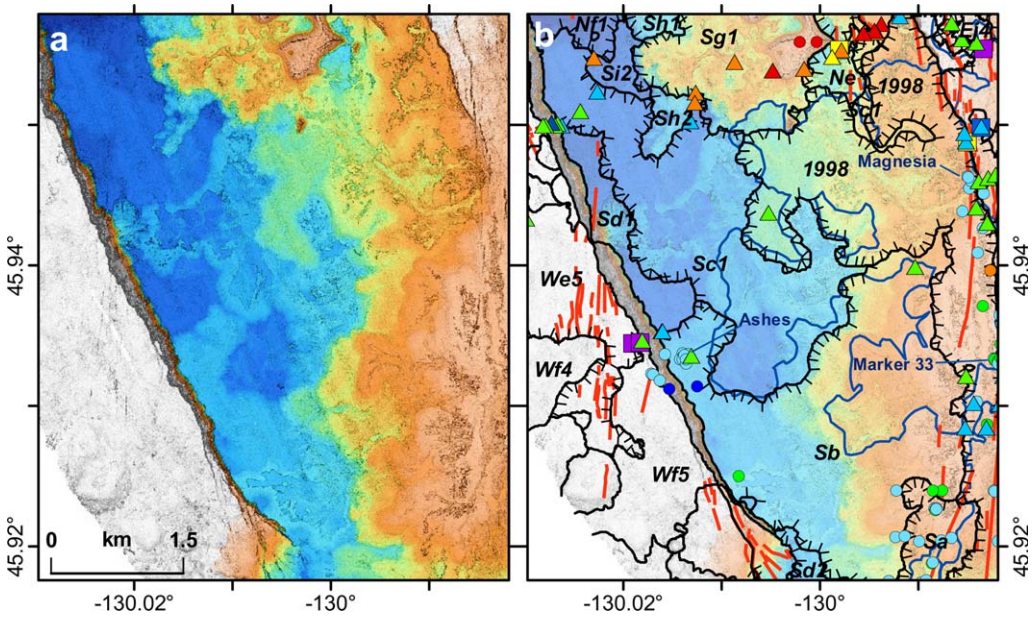

Figure 13. Close-up view of AUV bathymetry of the south caldera showing flow contacts. Flow unit labels and glass compositions are also shown on the southwest caldera rim. The 2011 flow (blue outline) now covers much of this area. The ASHES, Magnesia, and Marker 33 vent sites [*Butterfield et al*., 2004] are labeled. Histogram-equalized color ramp is −1570 m (blue) to −1500 m (orange).

imagery. Thus, this flow predates the 1998 flow by at least 16 years, but based on the glassy flow surfaces and lack of sediment, perhaps not by many years. It erupted from a series of at least 7 up to 14 m deep and up to 12 m wide *en echelon* fissures extending for 3.6 km that were reused by the 2011 [*Caress et al*., 2012a], but not by the 1998 eruption [*Chadwick et al*., 2013]. The N end of the deep, wide portion is located close to where the caldera rim lies buried (Figure 2). To the S this fissure defines the crest of the S rift. The flow advanced to the S on the SE side of the uppermost S rift zone, skirting kipukas *Sj1 and Sj2*. Little work has been done on the more distal SE parts of the flow that extend outside the AUV map coverage after flowing 2.3 km to the SE from the fissures.

[56] The next older flow is inflated lobate *Flow Sb* that underlies the ASHES hydrothermal field (Figure 13). It erupted from fissures that are now buried near the 1998 and 2011 fissures. The flow advanced first W and then NW along the west caldera wall, before turning slightly to the NE at its distal end. That distal end of *Flow Sb* under the ASHES hydrothermal field is inflated, much like the distal flow lobes of the 2011 [*Caress et al*., 2012a] and the 1998 flows [*Chadwick et al*., 2013]. The average flow composition in Table 2 excludes *Pisces* submersible sample xl1732-MCB that appears to be mislabeled or mislocated as it is chemically distinct from all other nearby samples. Three other Pisces samples (xl1730-2-3, xl1730-4, and xl1730-MC5; [*Chadwick et al*., 2005]) excluded from the average were collected in 1988 and may be proximal samples of this flow from sites subsequently buried by the 1998 flow. The flow, especially near the ASHES hydrothermal field, is covered in thin orange sediment. The widespread discharge of low-temperature fluids through cracks in the flow produces this orange sediment and makes use of pelagic sediment cover to estimate relative age problematic in this area.

[57] *Flow Sc1* (Figure 13) is exposed 1.3 km W of the Magnesia vent site and abuts the W caldera wall at its N distal end. Its proximal end was partially buried by the 1998 flow that reoccupied many of the channels in the flow (the channels are visible in SeaMarc side scan data collected in the 1980s, see *Embley et al*. [1990] and discussed in *Chadwick et al*. [2013]), as did the 2011 flow [*Caress et al*., 2012a]. *Flow Sc1* apparently erupted from a fissure located near the Magnesia hydrothermal vent site, and the inflated lobate flow advanced W, ponded, then continued NW, as determined from the extensive channel system. The ponding near the W caldera wall formed a large lava lake surrounded by low levees. The N levee breached and the flow advanced 2.25 km farther to the NW (Figures 13 and 14).

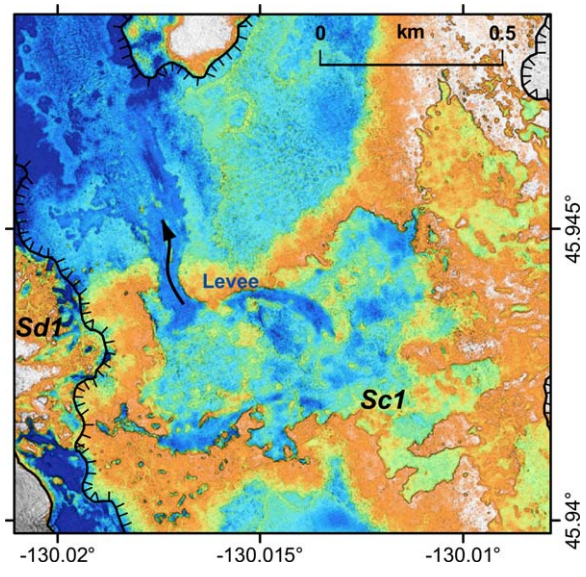

Figure 14. Close-up view of AUV bathymetry of part of *Flow Sc1*. The area shown is a distal inflated portion of the flow, but continued lava supply breached the pond levee on the northwest side and the outflow of lava cut a ~5 m deep channel (arrow) that fed several more large lobes of the flow. Color ramp is −1544 m (blue) to −1539 m (orange), with black and white deeper and shallower than the 5 m ramp, respectively.

[58] Where our ROV dives traversed the distal parts of *Flow Sc1*, sediment cover is inadequate to recover a core. However, a single radiocarbon age on core D270-PC50 (Table 1) from within the proximal contacts of the 2011 (and also the 1998) flow near the E caldera wall yielded a modern age prior to calibration (consistent with post-1950 bomb-derived radiocarbon in the dated foraminifera). This core, on such a young flow, could only be recovered due to 3 cm of orange-brown hydrothermal sediment, likely from both the 1998 and 2011 eruptions. The core site is characterized by abundant small spherical sponges and other benthic animals such as brittle stars, whereas the historical flow surfaces are devoid of such animals, so our interpretation is that we cored a kipuka of *Flow Sc1* within the 2011 and 1998 flows (Figures 13 and 11). The glass compositions for the two historical flows and *Flow Sc1* are indistinguishable (Table 2). Another large kipuka of *Flow Sc1* is identified from the AUV mapping, surrounded by lobes of the 1998 flow. *Flow Sc1* is younger than *Flow Ne*, dated at ~1650 CE.

[59] *Flow Sc2* is located S of the 1998K flow on the S rift (Figures 7b and 15). The flow is an inflated lobate flow with shallow lava ponds near the axis of the rift, and downslope to the SE it transitions into pillowed flow margins with shallow drain-out collapses. The flow has only thin sediment and so was assigned to the same time period as *Flow Sc1*.

[60] A small complex *Flow Sd1* abuts the base of the W caldera wall (Figure 13). The flow erupted from a short N-S fissure that cuts the N jumbled or hackly part of the flow; the eruptive fissure apparently continued up the W caldera wall but did not erupt on the rim. It is the southernmost young fissure in the caldera that is aligned with the north rift zone. The central portion of the flow consists of rough ridges radiating eastward from the base of the caldera wall and appears to be formed of lava that cascaded from the eruptive fissure located in the caldera wall. The southern inflated lobate flow lobe formed late in the eruption, has S-directed channels that originate at the base of the caldera wall. The flow ends just N of the ASHES hydrothermal field with an inflated lobate margin. The flow lacks adequate sediment to core, despite the widespread presence of orange hydrothermal sediment near the flow margin; it is, therefore, inferred to be more recent than 1650 CE. This lobe flowed south, apparently because lava piled up at the base of the caldera wall, forcing the flows to advance both N and S. It is the only flow in the southern 2/3 of Axial caldera to do so.

6.3.2. Type 2 Pillow, Inflated Lobate, and Inflated Sheet Flows Erupted 1220–1240 CE

[61] The two oldest dated flows inside the caldera, dated at 1223+76/-67 and 1236+69/-58 CE, are from the S part of the central complex of at least five plagioclase phyric flows (*Flows Sg1, Sh1, Sh2, Si1, and Si2;* Figures 7b, 9, and 13). The two ages are statistically indistinguishable, but the dated large inflated *Flow Sg1* is stratigraphically younger than dated *Flow Si1*. Stratigraphically consistent ages based on planktic foraminifera from core D75-PC43 on the northern lobe of *Flow Sg1* are 1766+85/-112 CE for 6–8 cm, 1423+77/-45 CE for 14–16 cm, and 1223+76/-67 CE for the basal 23–24 cm. The basal planktic age is corroborated by an age on benthic foraminifera from the same sample of 1186+107/-82 CE. The consistent ages of these three horizons show that bioturbation or other forms of sediment mixing have been minimal.

[62] *Flow Sg1* was previously described [*Appelgate and Embley*, 1992] using side scan, shipboard bathymetric data, and observations from ALVIN dive 2087. Our new data provide a more detailed map of the flow (Figure 12b) and we provide a modified interpretation of its formation in section

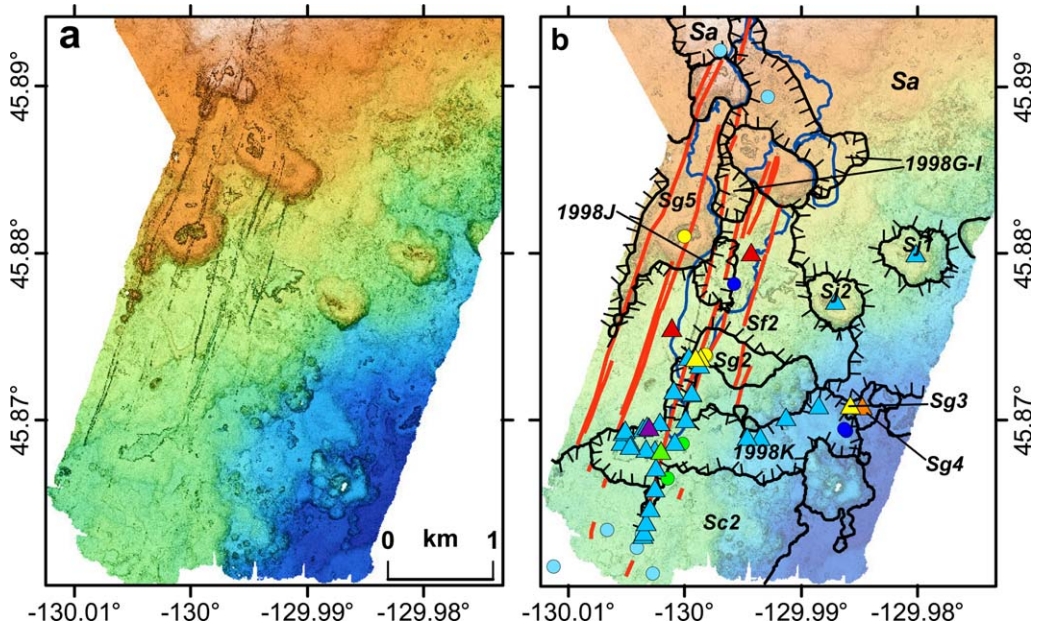

Figure 15. Close-up view of the AUV bathymetry of the south rift to the extent of our AUV mapping. Contacts of 1998 flows erupted from fissures G to K (labeled) from *Chadwick et al*. [2013]. The 2011 flow (blue outline) covers some of this area. Undated flows with high-MgO glass rinds shown in yellow to red assigned to the 1220–1305 CE timeframe based on composition and relative ages. Color ramp is −1821 m (blue) to −1675 m (orange).

7. The flow consists of a ~20 m thick inflated part, a sheet flow with irregular surface formed by inflation and deflation, a channel that is oriented roughly to the SW [*Embley et al*., 1990, Figure 8b], and a pillowed flow margin. The main inflated mound, with "lava-inflation clefts" in the terminology of *Walker* [1991] that served as hinge zones, is horseshoe shaped and open to the SW. The outward sloping surfaces are lineated or hackly sheet lava [*Chadwick et al*., 1999a], but they have been tilted upward at angles of 45° or steeper, in places forming a ridge with fractures as deep as 13 m at the crest. To the NW and S, small plateaus were uplifted, surrounded by deep fractures and outer steep down-tilted surfaces. The southern plateau surrounds a circular depression, which is the submarine equivalent of an inflation pit [*Walker*, 1991]. The strongly inflated portion abruptly transitions to the SW into a thinner inflated and drained flow, characterized mainly by a network of small shallow ponds with low levees and roofs that sagged. A channelized flow to the W, called the "Paw Flow" by *Appelgate and Embley* [1992], fed lava away from the thick inflated parts of the flow. The *Flow Sg1* margins are lobate to pillowed lava.

[63] *Flows Sh1 and Sh2* (Figure 9) may be parts of one flow that predates *Flow Sg1*. *Flows Si1 and Si2* may also be parts of another flow as they predate *Flows Sh1 and Sh2*.

[64] Along the S rift near the 1998G–K flows (fissures identified after *Chadwick et al*., 2013; Figure 15), there are several additional aphyric lobate to sheet flows. We place these in the same age group because of their Type 2 compositions and moderate sediment cover, where observed. The largest of these flows, *Sf2*, is a fluid sheet flow that made shallow ponds near the eruptive fissure and then advanced down the E flank of the rift, producing channels that drained and ending in inflated pillow margins. The flow is cut by eight fissures, consistent with its older age. Two samples were recovered using wax-tip cores so there was no opportunity to core sediment for dating. Observations made during *ROPOS* dive 494 show significant sediment cover consistent with assignment to this age category.

[65] Aphyric *Flows Sg2, Sg3*, and *Sg4* and cone *Sg5* (Figure 15) may date from this same time period.

6.3.3. Probable Pre-1220 CE Type 1 Pillow Cones

[66] Type 1 pillow cones *Sj1, and Sj2* have summits that inflated and cracked. The cones were sampled by wax-tipped rock corer and have not been observed. They are tentatively assigned pre-

1220 CE ages due to the degree of alteration of the recovered glass.

6.4. Prehistoric Lava Flows in Region E

[67] The lobate flows E of the historical flows (Figure 7c) are mostly younger than *Flow Ed* dated at 1398+71/-55 CE, and had inadequate sediment to core. Most of these flows are, therefore, likely to be more recent than 1650 CE despite having no contacts with the dated *Flow Ne*. Most flows (Figures 7c and 16) are inflated lobate flows with channels leading from shallow lava lakes that ponded above their eruptive fissures aligned with the uppermost S rift zone. Farther down the S rift, several undated aphyric flows have been grouped with dated Type 2 lava flows. Most flows in the northern part of region E are on the E caldera rim and predate formation of the caldera.

6.4.1. Type 1 Inflated Lobate Flows Erupted More Recently Than 1400 CE

[68] The youngest *Flow Ea1* issued from a fissure now buried beneath the 1998 and 2011 flows. The flow has numerous channels that first head SE and then E, where the flow continues beyond the mapped area. *Flow Ea1* has thin sediment cover, such that a 3–4 cm core was attempted but fell out of the tube. Sheet *Flows Eb1* to the south and *Eb2* to the north share no contact so their relative ages are unknown. *Flow Eb1* is a relatively narrow channelized sheet flow that heads E where it also continues beyond the AUV-mapped region. *Flow Eb2* is of limited extent, mainly along an eruptive fissure oriented 350° identified by numerous shallow, drained near-vent ponds. This flow has been neither observed by ROV nor sampled. *Flow Ec1* is similar in morphological character to *Flow Eb2*.

[69] *Flow Ea2* lies along the N rift zone outside the caldera (Figure 5) and is an extensive lobate flow that early reconnaissance dives and camera tows suggest continues along the N rift for at least twice as far as our map coverage. This flow has high backscatter and is younger than all surrounding flows. Dive observations show it is partly covered by thin sediment, numerous small spherical sponges, and occasional large sponges. We have used these observations to place it roughly in the same age group as *Flow Ea1*, the youngest flow E of the historical flows, but its age is not stratigraphically well constrained.

6.4.2. Inflated Lobate Flow Erupted ~1400 CE

[70] A stratigraphically important *Flow Ed* erupted 1398+71/-55 CE from fissures aligned with the S rift near the caldera rim and flowed E and SE around numerous kipukas. This flow provides a maximum age for the entire sequence of young lobate flows in the area as it underlies *Flows Ea1, Eb2, and Ec1*. It is characterized by bright side scan returns, a characteristic of all young sheet flows in the area and on the caldera floor. The bright side scan or high backscatter distinguishes it from most flows on the E and W rims of the caldera. This flow extends more than 2 km before it is outside the AUV mapped region and continues at least another 0.8 km to the SE based on its high backscatter from amplitudes of shipboard multibeam data (Figure 7c).

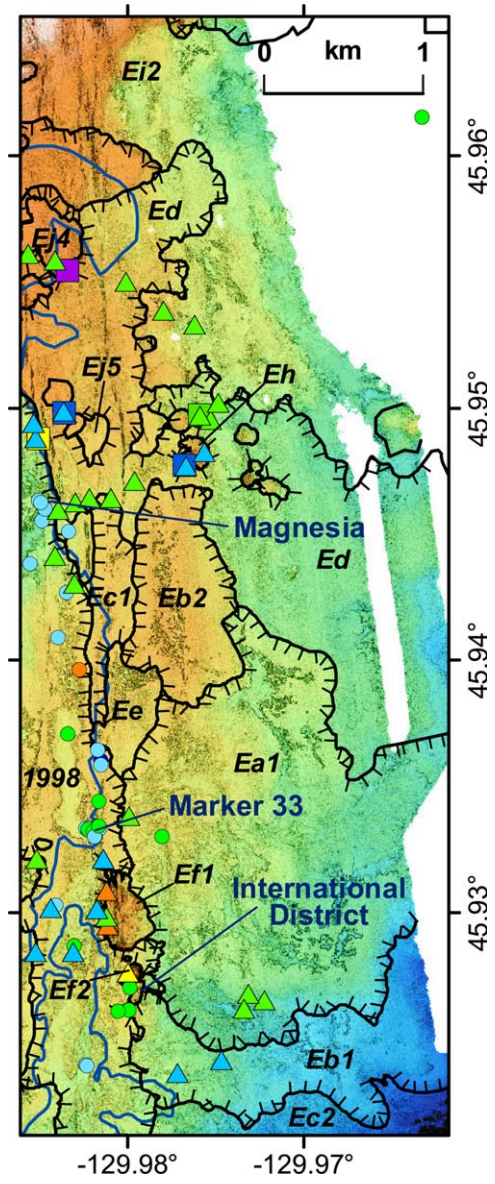

Figure 16. Close-up view of the AUV bathymetry of the southeast rim of the caldera. Hydrothermal vent sites Magnesia, Marker 33, and International District are labeled. Color ramp is −1555 m (blue) to −1490 m (orange).

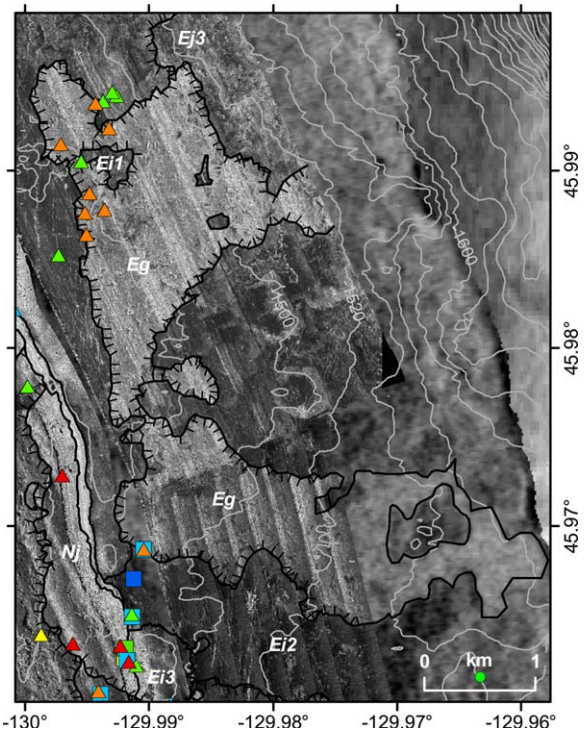

Figure 17. Side scan image of the east rim of the caldera. The data are side scan from the AUV (on the west 2/3) and backscatter data derived from amplitudes of shipboard multibeam data (on the east 1/3) with high intensity shown as light and low as dark. The flow outlines were identified primarily from intensity contrasts in the side scan data. Steeper flow margins on some older flows are also apparent as bright returns. The bright *Flow Eg* is dated at ~1260 CE and has thin sediment cover compared with the surrounding older flows that are covered by >1 m of clastic deposits. Contours in gray every 20 m.

6.4.3. Type 2 Flows Erupted ~1260 CE

[71] An extensive high-backscatter lobate *Flow Eg* on the NE to E central rim (Figure 17) erupted from a series of *en echelon* fissures that align with the S rift zone but cut through the E flank of the summit almost to the N end of the caldera. The N half of the flow was mapped from side scan data by *Embley et al*. [1990]. The contacts of the flow E of our AUV coverage were identified using backscatter data from more recent shipboard sonar data. It is the final of just four flow (in addition to 2011, 1998, and Flow Na) that is not partly covered by subsequent flows. The flow covers an area of 3.4×10^6 m^2 and has an estimated volume of 12×10^6 m^3, using an average flow thickness of 3.5 m determined for the 2011 flows [*Caress et al*., 2012a]. The flow encloses several kipukas and has two main lobes. The distal lobes are inflated pillow flows, commonly with small collapses in their centers, which help to define the flow contacts. Core D262-PC77 yielded a planktic age of 1264+72/-56 CE, within the ~1220–1305 CE range of the oldest dated flows from the caldera floor in regions N and S. Also like most Type 2 flows on the N and central caldera floor, this flow is plagioclase phyric. Widespread clastic debris with glass compositions matching *Flow Eg* was sampled by pushcore and vibracores during dive T1010 in 2005 [*Helo et al*., 2011]. These locally derived glass fragments contribute to the nearly 2 m thick clastic deposit near the NE caldera rim.

[72] Aphyric pillow cones labeled *Flow Ef1 and Ef2* (Figure 16) are aligned along the inferred, buried S caldera boundary. In addition, sample xl1730-6-7 collected by the *Pisces* submersible in 1988 from a location covered by the 1998 and 2011 flows (Figure 16) is distinct from other flows in or near the S caldera, with the exception of the two cones *Ef1* and *Ef2*. The sample presumably was collected from an otherwise unsampled *Flow Ee* to the east (Figure 16). We place *Flow Ee* in this age bracket based on the composition of the sample collected prior to emplacement of the 1998 flow.

6.4.4. Type 1 Pillow Cone Erupted ~410 CE

[73] A small pillow cone (*Flow Eh*, Figure 16) on the eastern flank yielded a planktic foraminifera age of 411+109/-123 CE. Lava flows with ages between ~410 CE and at least 31 ka BP have not been found on the caldera rim; *Flow Eh* is the oldest postcaldera lava dated during the study. Other older ages from region E, described in section 6.4.5, are minimum ages of the underlying, probably precaldera, lava flows as they date layers within the clastic deposit.

6.4.5. Type 1 Precaldera Inflated Lobate Flows and Pillow Mounds

[74] Sheet *Flows Ei1* (low backscatter areas on Figure 17), *Ei2, and Ei3* and pillow ridges *Ej1 and Ej2* (Figure 8c) flowed radially away from the summit. Although short push-core and vibracores were collected on these flows, none contained adequate foraminifera to date.

[75] Several cores provide minimum ages for the clastic section on the E side of the caldera. Core D79-PC70 was collected adjacent to a fracture cutting *Flow Ej4* where the upper layers of the thick clastic layer had eroded away, exposing deeper parts of the section. The 30 cm core could not penetrate the remaining section, and the unconsolidated and granular nature of the vitriclastic ash and lapilli made it especially difficult to recover as the glass shards poured from the core bottom

before the cores could be stowed. The 21–22 cm slice yielded an age of 6440+117/-113 cal yr BP, but as this was at an unknown depth in the section, it provides only a very minimum age of the underlying flow.

[76] Other cores in the clastic unit (D262 cores, Table 1) yielded much younger ages of 1327+46/-75 CE for a slice 17–19 cm deep, 1084+87/-103 CE for the base of a 25 cm long core and 1180+105/-84 CE for 17–18.5 cm deep in a 53 cm long core D262-PC45L, all on *Flow Ei2*. This last age has greater geological uncertainty because in order to have enough material, the analyzed sample was a mixture of planktic and benthic foraminifera, so we have used a ΔR-factor halfway between those for benthics and planktics to calibrate the age. The dated sample is just above a fine-grained green hydrothermal-clay rich layer containing pyrite fragments, which in this core extends from 19 to 45 cm depth [*Portner et al*., 2012]. This unit was deposited during a period of intense hydrothermal activity that ended ~895+93/-93 CE, as dated above a thinner layer of similar hydrothermal material in core D270-PC70. None of these cores reached the underlying flow, but the ages demonstrate how rapidly these glass-rich and hydrothermal-clay-rich clastics can accumulate, and how varied the thickness-to-age ratio can be (Table 1). Based on the ages of the cores from the E caldera rim, we can only conclude that the precaldera flows are >6.6 ka BP. Cores from the rim in region W to be described next indicate that this minimum age is too young by ~25 ka.

6.5. Type 1 Prehistoric Lava Flows in Region W

[77] Region W (Figure 7d) consists mostly of precaldera flows that flowed westward away from the present caldera wall. Sediment ages on top of these inflated lobate flows are as old as 31 ka BP. Several much younger flows with high backscatter erupted from fissures that may parallel the caldera-bounding faults. Two inflated lobate flows appear to be post-1450 CE and two other lobate flows are older and erupted from fissures ~2 km west of the caldera wall between 800 and 1000 CE.

6.5.1. Type 1 Inflated Lobate Flows Erupted Probably More Recently Than ~1450 CE

[78] *Flows Wa and Wb* on the NW rim of the caldera (Figure 7d) have high backscatter and are likely the two youngest flows on the W flank, but neither is dated. These flows have higher and more uniform backscatter than *Flows Wc and Wd*, which

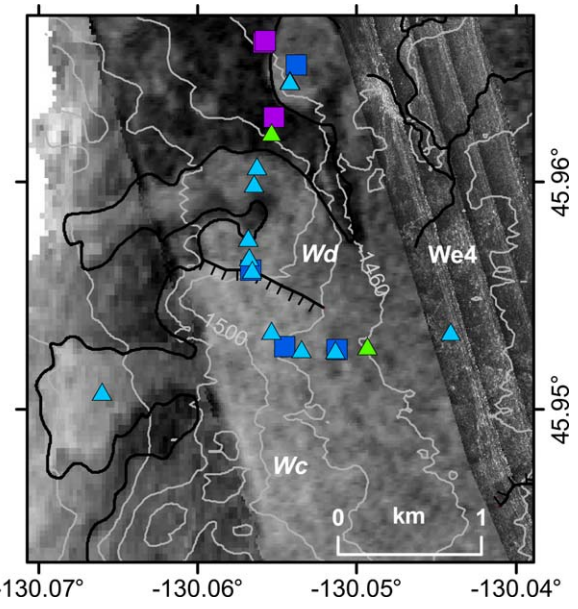

Figure 18. Image of the west rim of the caldera, mostly west of the AUV mapping. The grayscale shown in the western ¾ of the image is backscatter data derived from amplitude data of shipboard multibeam with light as high intensity and dark as low intensity, whereas that in the eastern ¼ is side scan collected by the AUV. The flow outlines are based on these intensity contrasts. The southern *Flow Wc* and northern *Flow Wd* are distinguished solely on their radiocarbon ages of ~800 and ~1000 CE, respectively. Their lava compositions are statistically identical. The eruptive fissures are not mapped as they are located west of the AUV coverage. Contours in gray every 20 m.

are dated at ~800 and ~1000 CE (see below). Cores on *Flow Wb* near the caldera wall contained too few foraminifera to date, but the flow has less sediment cover than *Flows Wc* and *Wd* and we infer that *Wa and Wb* are probably more recent than ~1450 CE, based on their sediment cover and benthic animal populations. *Flow Wb* drapes some fault block scarps (Figure 4a).

6.5.2. Type 1 Lobate Flows With Moderate-Backscatter Erupted 800–1000 CE

[79] Relatively young flows with moderate backscatter were identified in shipboard multibeam data on the W rim of the caldera, W of our AUV mapping coverage (*Flows Wc and Wd*, Figures 7d and 18). They were first sampled with a wax-tipped rock corer in 2009 and then dive D259 in 2011 explored and sampled them and the much older flows between their lobes. Glass-shard rich clastic deposits on the older flows are almost 1 m thick. Longer cores contain two black glass-rich layers with muddy glassy layers on top and between. Below the lower black glass-rich layer is foraminifera ooze with only minor glass.

[80] The flow lobes crop out through moderate clastic sediment cover. Ages on benthic foraminifera from cores D259-PC6, -PC65, and -PC70 yield ages of 809+100/-107, 1018+75/-98, and 986+61/-82 CE and a planktic age from core D259-PC2 is 789+96/-81 CE. The four ages may date a single flow that erupted ~900 CE, but the ages suggest that two flows with indistinguishable MgO contents may be present: a southern *Flow Wc* ~1000 CE and a northern *Flow Wd* erupted ~800 CE (Figure 18). These flows are older than any flows on the caldera floor or the two dated sheet flows on the E and SE rim, and erupted through unmapped fissures aligned with the N rift zone, or from fissures that parallel the caldera-bounding fault. These are the only flows identified on the W rim with moderate backscatter.

6.5.3. Type 1 Precaldera Lobate Flows

[81] Several cores were recovered from beyond the AUV mapping coverage and near the high-backscatter *Flow Wd* on the W flank (Figure 18). The bases of 55 cm long core D259-PC46L and 45 cm long core D259-PC59L yielded planktic foraminifera ages of 15,262+328/-405 and 16,081+688/-530 cal yr BP, and a nearby core D259-PC51L yielded duplicate planktic foraminifera ages from 62 cm of 19,483+108/-113 and 19,289+371/-171 cal yr BP. Again, the cores were not as long as the tube penetrated, so these ages are probably minimum ages of the underlying flow or flows, perhaps by 40–50%. Only a single lava sample was collected because clastic deposits bury nearly all of this flow.

[82] Farther N, near the caldera rim, *Flows We2* and *We3* (Figure 8d), are deeply buried by clastic deposits. Cores collected are all <25 cm long and foraminifera were too sparse to date. *Zonenshain et al*. [1989] report a radiocarbon age of ~12 kyr BP from the bottom of a 15 cm long piston core taken nearby.

[83] Sheet *Flows We4, We5*, and *Wf4* are covered by ~80 and 120 cm of clastic deposits along T1009 (supporting information Figure S1). Core recovery was always <~25 cm (see supporting information 4) and no dates have been obtained.

[84] Sheet *Flows We4, We5, and Wf5* were sampled on the rim just above the ASHES hydrothermal field (Figure 7d). *Flow We5* was erupted from a fissure obliquely intersecting, but truncated by, the west caldera wall. Core D256-PC59L (43 cm long) taken above *Flow We5* yielded a planktic foraminifera age of 12,838+169/-145 cal yr BP for the bottom 1 cm. The core penetrated about 90 cm, so the lower ~50% of the section was not recovered, and the age is likely significantly younger than the underlying flow. Nearby core D256-PC77L (39 cm long) yielded an age of 31,160+201/-194 cal yr BP from the core catcher (although the core did not recover the entire penetrated clastic section in this core) and is the oldest sample dated from Axial Seamount.

6.6. Lava Flows in the Caldera Walls That Erupted Before 31 kyr

[85] Traverses were made up the caldera wall during 6 ROV dives (T1010, D70, D71, D75, D256, and D262, supporting information Figure S1). The exposed flows vary in thickness and morphology, with drained lobate sheet flows, thin sheet flows, thick massive lobate sheet flows, and pillow lavas all represented. Massive flows in the NE, NW, and SW wall have jointing approaching columnar in thick massive flows. Each of the transects shows alternating near-vertical lava outcrops and angle-of-repose talus slopes creating a stairstep character to the walls. Ponds of clastic deposits between truncated flows were specifically sought to date the section, but none were observed. The basal outcrops and talus on NE, NW, and W walls are hydrothermally altered with bright orange deposits along fractures and coating surfaces that are now inactive based on lack of bacterial mat. The hydrothermally altered section is not exposed on the lower E wall.

[86] Many of the samples from NE (dive D70), NW (D71), W (D75), and E (D79) caldera walls lacked glass rinds. For this reason, seven of these lava samples were analyzed as whole rocks [reported in *Dreyer et al.* [2013]. These samples, and all new samples from the walls with glass rinds, have Type 1 major-element compositions similar to most of the flows sampled from the rims of the caldera beneath the thick clastic section, as well as the many sheet flows erupted since 1400 CE. Two samples (xl2085-2 and xl1728-4B; *Chadwick et al*. [2005]), which we infer to be from the walls or talus at the base of the walls, are Type 2 lavas, similar to those erupted on the caldera floor and upper rift ~1220–1305 CE.

7. Discussion

[87] The data presented above allow us to examine: (1) aspects of lava flow emplacement, (2) the

evolution of eruptive fissures, (3) the longevity of hydrothermal fields, (4) the early history of the summit when the caldera formed, (5) the post-400 CE volcanic stratigraphy and eruptive history of the summit region, and (6) the eruption recurrence intervals of the summit region on several time scales. These data also provide a framework for evaluating changes in magma generation and plumbing in Axial Seamount over time, as developed in *Dreyer et al.* [2013] and *Helo et al.* [2011], and the interplay of volcanic and hydrothermal processes as recorded in the clastic section on the caldera rims, as developed in *Portner et al.* [2012].

7.1. Lava Flow Emplacement

[88] The high-resolution mapping data provides insight into emplacement of the spectrum of flow morphologies by revealing the spatial architecture of the lava types that comprise each flow type. Some interpretations based on the high-resolution mapping data follow, but this is not intended as a comprehensive evaluation of flow emplacement processes. Much of what we observe has been described previously, but has generally lacked the full 2-D distribution of lava morphologies within the entire flow. The different morphologies, with the exception of the inflated sheet flow described below, are illustrated in *Chadwick et al.* [2013, Figure 2].

7.1.1. Inflated Lobate Flows

[89] Most of the flows in and near the caldera, including both historical flows, are inflated lobate flows, but the range of flow architecture shown by the many flows mapped at the summit far exceeds the range seen in the two historical flows. Larger inflated lobate flows, including both historical flows, generally have lava ponds surrounding the eruptive fissures, and smaller flows may have a string of collapse pits delineating an inferred fissure. These ponds drained down complex channel systems. The channels in turn drained as the flows advanced downslope, and often are floored with hackly or lineated sheet flows [*Chadwick et al.*, 1999a]. The drained ponds above the eruptive fissures and the drained channels typically in the near-vent portions of the flows are surrounded by lobate flows. The lobate flows adjacent to the channels are commonly hollow underneath (perched lava crusts) with abundant lava pillars [*Gregg and Chadwick*, 1996; *Chadwick*, 2003; *Engels et al.*, 2003]. Farther from the drained channel, the molten core of the lobate flows no longer drained to created collapses. Farther still in length and width, the lobate flow textures grade into pillow lavas. The widths of these different facies vary widely from flow to flow, with the channel facies nearly absent (e.g., 2011 flow in the caldera) to comprising most of the flow (e.g., *Flow Sc1*, *Flow Nc*, *Flow Ne*, 1998D–F). Similarly, the lava facies also vary along the advancing inflated lobate flows such that channels remain open (drained) for variable distances from the eruptive fissures. These differences are caused by variations in emplacement processes that we discuss below.

[90] The distal lobes are commonly inflated (e.g., 1998 and 2011) forming what *Chadwick et al.* [2013] termed inflated pillow flows. These distal flows form by the processes outlined by *Hon et al.* [1994] for subaerial Kilauea lavas where molten lava is injected under the crust and thickens the flow from within. As at Kilauea, this process is mainly observed far from the eruptive fissures or vents and on gentle slopes. Distal inflated flows can take on a range of morphology depending on the slope. On nearly flat slopes, as on much of the caldera floor, the pillowed margins of the lobe inflate and thicken, and then the flow interior is slightly inflated above the thickness of the pillowed margins. The surfaces often remain smooth and may sag slightly, suggesting the crust is thin and still plastic during this process. This style of inflation is observed in the 2011 [*Caress et al.*, 2012a] and 1998 [*Chadwick et al.*, 2013] flows, near the distal ends of the lobes emplaced to the west into the caldera from the northernmost fissures near Magnesia vent site (Figure 13).

[91] The 1998 and 2011 distal pillow flows that descend steeper slopes to the south and southeast outside the caldera have a slightly different structure where the advancing flow inflates. Instead of further inflation of the core, the core collapses as the flow continues to slowly advance and spread after the influx of lava has ceased. Collapse pits and depressions a meter or more deep are lined with shelves and veneers of lava left as the flow drained. This type of flow lobe in the 1998 flow formed on the south rift from fissure K [*Chadwick et al.*, 2013, Figure 16], and is also widely seen on the flanks of the caldera where flows erupted prior to formation of the caldera advanced down steeper slopes. We emphasize that what the mapping data illuminate is the entire architecture of these complex flows, which in turn allows us to envision the sequence of events and processes that

constructed individual flows. What is remarkable at Axial is that so many flows have had similar histories and distribution of facies, and most are similar in overall architecture to the 1998 flows [*Chadwick et al*., 2013] or the 2011 flows [*Caress et al*., 2012a].

7.1.2. Pillow Mounds

[92] Not all flows near the summit of Axial Seamount are inflated lobate flows. There are also pillow mounds, especially along the south rift and south caldera rim, but also in the caldera center where many of the high-MgO flows are pillow mounds that erupted in between the extensions of the south and north rift zones along the east and west sides of the caldera floor. As noted by *Yeo et al*. [2013], pillow eruptions do not necessarily form a chain of rooted mounds or pillow ridges aligned solely along the eruptive fissure. These flows also can spread laterally and form mounds near the fissure, but offset from it by perhaps a hundred meters. This observation, which is applicable for the pillow mounds in the caldera center at Axial, suggests that the mounds may also harbor a molten core that can transport lava laterally to feed rootless mounds.

7.1.3. Inflated Sheet Flows

[93] Axial has yet another flow type not described by *Chadwick et al*. [2013] that we are calling an "inflated sheet flow." This term describes the tumulus-like features such as *Flow Sg1* (Figures 11 and 12b) described by *Appelgate and Embley* [1992] and also described based on these AUV data and ROV observations by *Paduan et al*. [2009]. *Flows Ni1 and Ni2* on the north central caldera floor are similar although smaller in size. Their structure and appearance are indeed identical to tumuli [as noted by *Appelgate and Embley*, 1992], but they form by a different process of inflation since their inflated parts are the shallowest parts of the flow. Therefore, these must be perched on top of eruptive fissures/vents rather than being secondary flow features like tumuli formed downslope from eruptive vents. The tilted slabs on the sides of these features usually consist of lineated or jumbled sheet lava of near-vent morphology, and the lava crusts can be more than 1 m thick. We propose that these features form during the waning stages of eruption of a sheet flow and result from slow continued injection of molten lava from below that lifts the thick sheet flow crust and cracks it to form the observed structures in a manner described for on-land flows by *Walker* [1991].

7.1.4. Factors Controlling Flow Morphology and Architecture

[94] Morphology of submarine basalt flows is related primarily to extrusion rate [*Griffiths and Fink*, 1992; *Greg and Fink*, 1995; *Gregg et al*., 2006] and to slope [*Gregg and Fink*, 2000; *Greg and Smith*, 2003; *Fundis et al*., 2010]. The role of steep slope in elongating the shape of terrestrial pahoehoe flows is widely recognized and plays a similar role for elongating submarine pillow lavas [e.g., *Moore*, 1975; *Clague and Paduan*, 2009]. However, it also exerts strong control on the architecture of sheet and lobate flows: on the width of the channel system or lobate and pillow margins; how far from the fissures the drained channel extends downslope; and if the distal pillow flows inflate and then drain or continue to inflate. Extrusion rate is related to a combination of magma viscosity, dike width, and magma buoyancy or bubble content [e.g., *Head and Wilson*, 2003]. Magma viscosity is itself controlled by melt temperature and composition including volatile components, and crystal and bubble content [e.g., *Shaw*, 1972].

[95] A recent evaluation of magma viscosity and its relation to flow morphology, and therefore, to extrusion rate, for lavas from the Alarcon Rise [*Martin et al*., 2012] shows little correlation. As expected, lavas from pillow mounds all had higher viscosities due to generally lower melt temperatures and high crystal contents, but lavas from inflated lobate or sheet flows had a wide range of viscosities that overlapped the range for pillow lavas. Since viscosity does not correlate with extrusion rate (inferred from flow morphology), dike width, and magma buoyancy or bubble content, neither of which is straightforward to assess, must play important roles. Clearly, some of the rapidly erupted inflated lobate flows on Axial erupted through unusually wide dikes (e.g., *Flow Sa*), as seen by the gaping fissures remaining after their eruption. However, *Clague et al*. [2009a] also suggest that abundant pyroclast production correlates with rapid extrusion rate sheet or lobate flows compared to sparse pyroclast production for eruptions that produced pillow mounds. This relationship suggests that magma buoyancy (amount of exsolved bubbles) is a significant factor in determining magma ascent and extrusion rates, and therefore, to flow morphology. Formation of sheet and lobate flows may require the combination of low viscosity magmas, wide feeder dikes, and high magma buoyancy caused by abundant exsolved bubbles.

7.2. Evolution of Fissures

[96] Slope may play a significant role in the evolution of the eruptive fissure system. One of the striking features of the historical and several other young eruptions such as *Flow Sa* around the Bag City hydrothermal field at Axial are the open fissures that remain when the eruptions are over. Several of these open fissures in the 1998 flow (such as around the Marker 33 site, Figure 16) were located within small closed depressions, suggesting that lava drains back down the eruptive fissures when activity along fissures ends, as also described from the East Pacific Rise [*Fornari et al*., 2004].

[97] The geophysical data, especially for the 1998 eruption [*Dziak and Fox*, 1999; *Fox*, 1999] suggest that the fissures progressed from north to south down the S rift zone. This configuration is identical to eruptions such as the 1984 eruption on Mauna Loa, where activity at the initial fissures stopped as the eruption migrated down the NE rift zone [*Lockwood et al*., 1987]. Axial Seamount eruptions apparently do the same. This is a mechanism to shut off the eruption at the shallowest fissures abruptly, leaving the fissures as open cracks, whereas down the rift, the fissures are filled with lava when the eruption is over. At Axial, the fissures on the south rift zone (Figure 15) show extensional ground cracking, but in general, the eruptive fissures are filled by lava by the end of the eruptions. Inflated sheet flows are apparently restricted to gentle slopes and cover their fissures in new lava. Pillow ridges, regardless of slope, bury their underlying fissures.

[98] The observation that fissures within the caldera are left as open cracks when activity ceases at those fissures is probably key to them being reoccupied by the subsequent eruptions. Such reoccupation clearly happened with the 2011 eruption using fissures from the 1998 eruption [*Caress et al*., 2012a], and also with the 1998 eruption using fissures from eruptions that had produced *Flows Sc1 and Sa* [*Chadwick et al*., 2013]. When the same fissures are used again, lava pools in the same lava ponds around those fissures, and flows along the same drained channels from the previous eruption. To break this cycle, a new eruption using the same fissures may need to be restricted to the summit, so that the lavas are not drained into deeper parts of the dike and the fissures are clogged at the end of an eruption. The general lack of deep, open fissures suggests that eventually this takes place, forcing the next eruption to break new ground to the surface. In eruptions where the propagating dike intersects open fissures at some greater depth below the surface, the eruption may have higher effusion rates and, due to rapid rise rates and decompression, may also produce more pyroclastic debris than in eruptions where the dike has to propagate all the way to the surface before the eruption can begin.

7.3. Distribution and Duration of Hydrothermal Activity

[99] The largest of the vent fields, at International District, is located near the inferred eruptive fissures for *Flow Eb1*, one of the younger post-1650 CE flows, and adjacent to the margin of the 1998 flow. The other fields are found on the flows we interpret to be younger than 100 years, so the vent fields should also be equally young.

[100] Cores on the east rim contain a variably thick green hydrothermal layer that probably formed as fall-out from chronic plumes. The uneven distribution of this unit around the caldera implies that bottom currents preferentially flow toward the east. It appears to have formed during a period prior to 895+93/-93 CE, as determined from a date at the top of the layer. This may be a time period when eruptions were less frequent than they have been more recently, providing the tantalizing observation that frequent and voluminous eruptions may correlate with periods with minimal hydrothermal activity and infrequent eruptions may correspond to periods of intense hydrothermal discharge, as observed at Endeavour Ridge. Better age control on the start and end of this period of active and widespread hydrothermal activity at Axial, represented by the gray-green layer in the cores, should be possible with more and longer cores, especially from the east caldera rim.

[101] The rarity of chimneys mapped at Axial Seamount contrasts with the ~950 chimneys identified at Endeavour Ridge [*Clague et al*., 2008] and over 110 along the Alarcon Rise from 1 m data collected using the same AUV [*Paduan et al*., 2012b]. Only chimneys at International District would be identified as such from the mapping data alone without prior knowledge that chimneys were present in the area. The AUV mapping confirms that large sulfide chimneys are rare at Axial Seamount, as determined by prior extensive exploration to locate hydrothermal discharge sites [*Baker et al*., 1990; *Butterfield et al*., 2004].

7.4. Early Summit History: Caldera Formation and Filling

[102] Most flows on the outer rims of the caldera flow radially away from the caldera wall and channels in them are truncated by the caldera-bounding faults. These relations indicate that the flows on the rim were emplaced prior to caldera formation. Formation of the caldera may have occurred within a few hundreds of years after the summit overflows were emplaced, as observed at Kilauea where a series of summit overflows are dated to 1290–1470 CE [*Clague et al*., 1999; *Neal and Lockwood*, 2003] and the subsequent explosive eruptions marked the development of the present caldera that began no later than 1470–1510 CE [*Swanson et al*., 2012]. Mauna Loa has a similar history with the last period of summit overflows ending about 1200 CE and followed by formation of its caldera [*Lockwood and Lipman*, 1987]. At Kilauea and Mauna Loa, the end of the summit overflows roughly coincides with caldera formation.

[103] If we assume that Axial Seamount had similar timing between the end of summit overflows and caldera formation, the youngest flows on the rim that are truncated by the caldera would correspond to the formation of the caldera, and the youngest and oldest summit overflows would differ by only a few hundred years. Coring on the rims of Axial caldera has been exceedingly difficult (see supporting information 2.3 for details on coring program) and none of the cores has recovered the entire sediment section, so all yielded minimum ages. The oldest age, 31.2 cal kyr BP from a core on *Flow We*, provides a rough minimum age for the formation of the caldera. However, this age is from the base of a core that only recovered about 50% of the sediment section that it penetrated, so the age of the underlying flow could be as much as twice as old as the determined age and formation of the caldera could have occurred 60 ka ago. We have determined a series of ages between 12.8 and 19.4 cal kyr from the bottoms of other cores taken on the rim, all of which also recovered slightly more than half of the penetrated sediment. These results are consistent with the 31.2 ka age being our best estimate of the minimum age of the caldera. In order for this to be correct, core D256-PC77L (Table 1) would have sampled the upper ~35 cm of the roughly 85 cm section, then continued insertion resulted in no recovery until the very bottom, where a few cm were recovered from on top of the underlying lava flow. That core was inserted slowly against a lot of resistance, as usual, and experienced unusually rapid, easy insertion at the end. We think friction of the glassy material in the core barrel had prevented the core from entering the tube elsewhere, despite penetration by the core barrel. An alternate explanation for the limited recovery would require ~50% compaction of the sediment in the core tube, which seems unlikely for such glass-rich sediment. Dating of long cores to be collected in the future will hopefully remove this significant ambiguity.

[104] The caldera might have formed during a single collapse event and has been filling for the entire 31 ka since it formed. This would be dissimilar to the deep caldera on Fernadina Volcano in the Galapagos Islands that deepened from 800 to 1100 m in 1968 [*Simkin and Howard*, 1970]. The Axial caldera was most likely not as deep as that at Fernadina since Fernadina's caldera is the deepest of those at basaltic volcanoes, so the maximum volume of the Axial caldera after it formed 31 ka ago was 25×10^9 m^3 (area of Axial caldera floor of 22.5×10^6 m^2 $\times$ depth of 1.1 km). The largest and smallest documented flows at the summit of Axial are 27×10^6 m^3 (for 2011 flows) and 7×10^6 m^3 (for *Flow Na)*. To fill this maximum caldera would require an eruption recurrence interval between 9 and 33 years for the elapsed 31 ka since the caldera formed, if there were no events that deepened the caldera after its formation. It seems more likely that the caldera floor at Axial dropped repeatedly during large eruptions down either of the rift zones that would have depressurized the summit, as proposed by *Holcomb et al*. [1988] for Kilauea's caldera or during flank eruptions as proposed by *Simkin and Howard* [1970] for Fernadina's. Axial also had a large-volume eruption ($>5 \times 10^8$ m^3) along the deepest portion of the south rift zone where a 90 m deep lava pond complex formed [*Paduan et al*., 2005, 2012a] with an extensive sheet flow adjacent to it. Another similar large-volume pond complex exists near the base of the north rift zone, but it remains unexplored. The south rift pond complex is still less than 1/5 the volume of the present caldera, so is not likely to correlate with an episode of caldera formation, but perhaps it coincided with an episode of caldera deepening.

[105] The flows erupted in and near the S caldera and upper S rift have spilled into the caldera and buried the southeast rim (inferred location shown in Figure 2). The floor of the caldera today, which deepens to the north (Figure 3), may reflect the

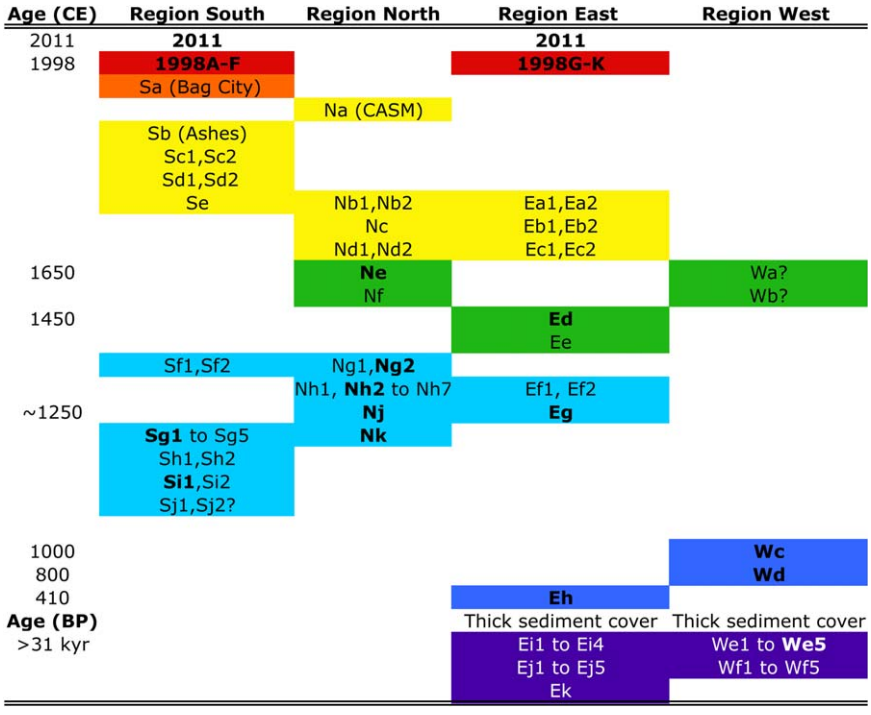

Figure 19. Flow unit correlation chart for Axial Seamount. The flows are arranged in age sequence for each of the four regions, correlated between those regions and the colors match those on Figure 20a. Dated flows are shown in boldface. All ages are in years CE except the oldest age group that are in calibrated kyr BP.

much more frequent and voluminous eruptions that have taken place along the upper south rift compared with the north rift. The flat pond and rim surfaces of *Flow Nd2*, which were presumably horizontal when it was emplaced, are gently tipped downward to the north. That subtle tipping could be due to trapdoor motion, as proposed by *Embley et al*. [1990], but could also be caused by inflation of the central caldera floor as the magma reservoir fills [*Chadwick et al.*, 2012] or by emplacement of shallow sills. That the tipping has occurred in <300 years supports deformation as the cause of the subtle tilting and suggests that the overall slope of the floor up to the south is because of more voluminous young activity at the south end that has simply filled the southern caldera more than the northern end.

7.5. Post-410 CE Summit History: Eruptions on the Caldera Floor and Upper Rift Zones

[106] The combination of high-resolution mapping data, relative ages, and some absolute ages has allowed us to reconstruct the structural and eruptive history at the summit and uppermost rift zones in much the same way that geologic maps are constructed for subaerial volcanoes. We have combined the maps of the four regions from Figure 7 to produce a stratigraphic correlation of map units (Figure 19), and the geologic map (Figure 20a), which is color coded to match the correlation chart. In addition, the average flow compositions and crystal contents from Table 2 are shown on the same flow-by-flow map in Figure 20b. The key results are that the compositions of the lavas and locations of eruptive fissures have changed in a recognizable way over time. The stratigraphy at the summit defines a style of activity that changes through time and space. Some of these changes entail significant changes in magma composition, but most do not. The history of activity is presented from most recent to oldest, as more recent eruptions are displayed most completely, whereas older lava flows tend to be partly covered by subsequent flows.

[107] All flows more recent than 1650 CE are aphyric and chemically nearly identical Type 1 lava, and erupted from two main loci. The youngest group of flows, all probably 20th and 21st century, erupted along the uppermost S rift zone and its continuation along the SE edge of the caldera (Figure 20a) and include the flows erupted in 2011 [*Caress et al*., 2012a], 1998 [*Chadwick et al*.,

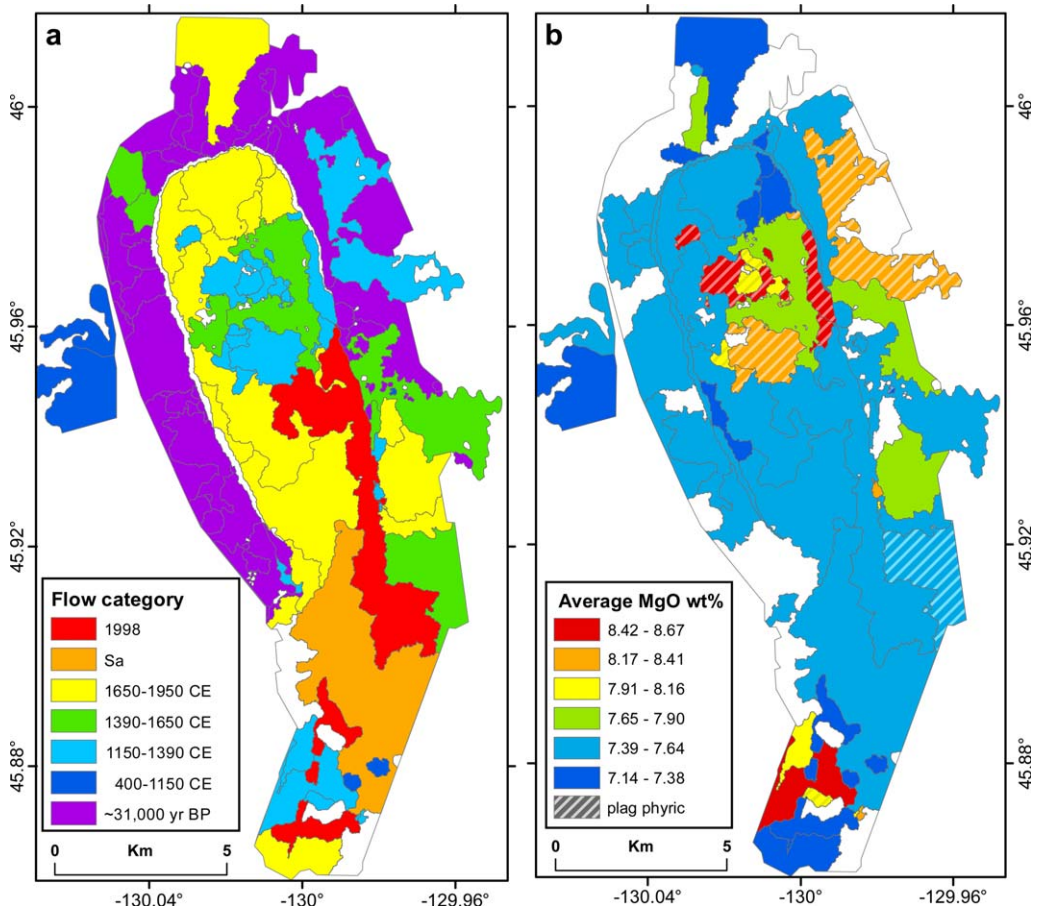

Figure 20. Summary maps showing the four parts of Figure 7 combined into (a) map by flow age grouped with color ranges as in the stratigraphic correlation chart (Figure 19) and age date symbols in previous figures and (b) map of flow composition, as average MgO (in wt%), with striped areas representing plagioclase phyric flows. All lavas on the caldera floor are more recent than about 1220 CE, and only rare flows on the rims have occurred more recently than ~410 CE with the rest of the rim formed from flows erupted prior to caldera formation, perhaps as long ago as 31 ka BP. Most of the flows are aphyric with low-MgO glasses (<7.6 wt%). Mostly plagioclase phyric flows with higher glass MgO (>7.9 wt%) erupted during a relatively brief period in the history of the volcano from ~1220 to 1305 CE.

2013], *Flow Sa*, and *Flow Sb*. Prior to that, and perhaps overlapping with it, from perhaps 1650 to 1800–1850 CE, similar intense activity occurred on the north caldera floor and rift. Around 1650 CE, a singular eruption of slightly more primitive, lava emplaced *Flow Ne* from a fissure along the west edge of the south rift zone across the caldera floor. Activity was focused on the upper south rift outside the caldera from 1400 to 1650 CE. All the post-1400 CE lavas are aphyric, slightly enriched (Type 1), with glass containing <7.6% MgO.

[108] Evidence for activity near the summit is lacking from 1305 to 1400 CE. Higher-MgO (hotter), phyric to ultraphyric, depleted lavas (Type 2) erupted from vents in the central caldera, and as an extensive sheet flow from fissures on the east rim of the caldera from 1220 to 1305 CE. This period is well dated with seven ages from nine cores ranging from 1305+91/-67 CE for *Flow Nh1* to 1223+67/-76 CE for *Flow Sg1* (Table 1, Figures 7a and 7b) and all the determined ages from the core bottoms overlap within their 2σ uncertainties. During the same time period, we infer construction of several small aphyric, but still high-MgO pillow mounds along the trace of the south caldera fault and of a few smaller sheet flows on along the upper south rift. This brief period of activity appears to have produced all the more depleted, more mafic, Type 2 lavas found near the summit and was preceded and followed by eruption of aphyric, less depleted, less mafic Type 1 lavas.

[109] From 1000 to 1260 CE, evidence for activity near the summit is lacking. Two (or maybe a single) lobate flows erupted through fissures to the

west of and parallel to the north rift zone or concentric to the west caldera wall between 800 and 1000 CE. The earliest postcaldera activity preserved and sampled near the summit occurred about 400 CE when a small pillow mound formed beyond the southeast caldera rim (*Flow Ej4*).

[110] Evidence for eruption of lava flows at the summit before 400 CE is missing until at least 31 ka, and possibly 60 ka, which is represented by summit overflows exposed only on the rims of the caldera. Younger ages on the rims of 6.6–19.4 ka BP are most likely minimum ages as they are from within the sediment section. These lavas that crop out on the summit outside the caldera and in the caldera walls are Type 1 and generally similar to those erupted since 1400 CE. Volcanic activity during this long period must have been restricted to the caldera floor, and possibly to the rift zones. The activity at the summit is recorded solely in clastic deposits rich in basalt glass shards that drape the rims of the caldera. Lava flows erupted in the caldera during this period, if any, were buried by younger flows. Long (1 m) push-cores collected during dives D256, D259, and D262 reveal several ~15–18 cm thick pyroclastic layers [*Portner et al*., 2012] interstratified with light brown sediment. These cores should contain detailed records of the magmatic and hydrothermal history of Axial Seamount in the long period between ~410 CE and >31 cal kyr BP flows beneath the clastic unit.

[111] This general pattern of shifting activity through time is familiar from other volcanoes, such as Kilauea, where *Holcomb* [1987] proposed cyclic loci of eruptive activity from summit to rifts, periods of intense activity and inactivity, and frequent caldera formation and filling on similar multihundred year timeframes. The biggest difference is that eruptive activity and caldera formation at Axial Seamount are less frequent than at Kilauea, and that the two volcanoes have different crustal stresses that control their activity.

7.6. Eruption Recurrence Interval at Summit

[112] The analytical errors inherent with the radiocarbon dating—generally in the ±80 year range—precludes placing tight estimates on recurrence intervals or periods of activity in different parts of the caldera and upper rifts. With that caveat in mind, there are ~24 discrete lava flows in the summit region, including the two historical eruptions, since ~1650 CE. The temporal distribution of these 24 eruptions is not known, but this equates to an eruption recurrence interval of 11–19 years, including the 2σ errors on the 1650 CE dated flow. The lavas produced during this period are relatively low-MgO (<7.6 wt%) aphyric lavas. This recurrence interval is statistically identical to the elapsed 13 years between the 1998 and 2011 eruptions and within the range estimated by *Nooner and Chadwick* [2009] based on rates of uplift in the caldera following the 1998 eruption. It also implies that in the last 100 years, it is likely that there were ~6–7 eruptions near the summit of Axial Seamount, and that all the youngest flows, including the *Flows Sa* at Bag City, *Sb* at ASHES, *Sc1* at Magnesia, and *Na* at CASM, might be less than a century old. It also implies that the eruption prior to the one in 1998, the Bag City *Flow Sa*, most likely occurred in the 1970s or 1980s, perhaps just a few years prior to the initial submersible exploration at the summit [*Chase et al*., 1985] and the collection of the SeaMarc II side scan data [*Embley et al*., 1990].

[113] From ~1305 to 1650 CE, there was little activity and no dated and mapped flows in the caldera. There was a single dated flow on the southeast rim and several other flows on the NW, N, and SE rims that we interpret erupted in this general time period. The period ~1220–1305 CE appears to have been a time with more frequent activity with seven dated and 17 more eruptions in <245 years including the 2σ errors on the bracketing ages, but of eruptions of higher MgO (8–8.7 wt%), predominantly plagioclase phyric lava. The eruption recurrence interval during this period was <10 years. This of course assumes that there are no additional flows that have been buried by subsequent flows, that our age data measure the entire period when high-MgO lavas erupted, and that the many small mapped lava flows were each independent of one another.

[114] If one looks at the entire post-1220 ± 80 CE period, there were at least 48 lava flows erupted at and near the summit, and the recurrence interval was 15–18 years. If we consider only the 35 flows within the caldera during this same time period, then the intracaldera recurrence interval is 20–25 years. These numbers, while rough, suggest that Axial Seamount has been in a phase of more frequent and larger eruptions since about 1650 CE, than during the preceding ~430 years. The recurrence interval at Axial Seamount's summit is much shorter than the five eruptions unevenly distributed during 370 years determined for the southern East Pacific Rise by *Bergmanis et al*. [2007].

The recurrence intervals estimated above suggest that the OOI regional scale nodes (RSN) observatory currently being installed in the S and central caldera of Axial Seamount will most likely be in place to capture the next eruption in unprecedented detail.

8. Conclusions

[115] Bathymetric mapping at 1 m lateral resolution collected using an autonomous underwater vehicle was coupled with 236 new geochemical analyses of glass rinds on lava samples, relative flow age relations, and absolute radiocarbon ages from 29 cores on top of flows to construct a geologic map of the summit of Axial Seamount. The mapping data show that all flows on the caldera floor are more recent than 1220 CE and that about 50% of them are more recent than 1650 CE. Lavas in and near the caldera that erupted since 1400 CE are aphyric, have glass rinds with 7.2–7.8 wt% MgO, whereas lavas erupted between about 1220 and 1305 CE have glass rinds with 7.9–8.7 wt% MgO and can be either aphyric or plagioclase phyric to ultraphyric, depending on their location on the seamount and within the flows. In 800–1000 CE, a few aphyric flows on the west rim had glass rinds with 7.4 wt% MgO. The reasons for these changes in lava chemistry over time are beyond the scope of this paper, but are explored in *Dreyer et al.* [2013].

[116] There is no clear record of lava flows at the summit between 410 CE and ~31 ka (or perhaps ~60 ka) when the collapse of the caldera most likely occurred. The long period of time without summit lava flows could indicate a general lack of volcanic activity at Axial Seamount, a shift of activity to the rift zones, or low-flux activity confined to the caldera floor where the flows were buried beneath more recent flows. There was clearly some activity at the summit, as the ~1–2 m thick sedimentary deposits on the caldera rims are largely composed of glass fragments produced by intense pyroclastic activity. Further work on the stratigraphy of the sedimentary section coupled with additional radiocarbon dating within those deposits should clarify the timing of volcanic activity in the caldera during this long period of time.

[117] The collapse of the caldera marks the end of summit eruptions with flows advancing radially outward from a summit shield. Difficulties in collecting the 1 m+ length cores of clastic debris on these old caldera overflows leave some uncertainty as to the timing of caldera formation, although the orientation of channels leading right to the top of the caldera wall (where they are abruptly truncated) attest to a precaldera period(s) of summit overflows.

[118] Most of the younger flows near the summit, and especially those in the caldera, are inflated lobate flows with complex drained lava ponds surrounding their eruptive fissures, drained channels leading away from the fissures, and lobate and finally pillow lavas toward the flow margins. The interior of the flows inflated and then usually deflated as the flow advanced. The period defined by flows dated in the range 1220–1305 CE is characterized by higher MgO and mostly phyric (Type 2) flows that are mainly located in the central caldera and erupted from vents not aligned with either the N or S rift zones that hug the east and west walls of the caldera and adjacent rim. These flows include pillow mounds and sheet flows that inflated as the eruptions waned. Three flows on the flanks erupted between 800 and 1400 CE. The most recent is on the east rim and the two older flows are on the west rim; all are defined by their high backscatter in side scan or multibeam amplitude data compared with the surrounding flows that are covered by 1–2 m of clastic deposits.

[119] Axial Seamount has widespread low-temperature hydrothermal venting, but sulfide chimneys large enough to identify in the mapping data are restricted to roughly a dozen chimneys at the ASHES and International District vent fields. Chimneys at CASM can be seen in the data, but without prior knowledge of their presence, would not be identified. The main hydrothermal vent fields occur on top of some of the youngest flows mapped at Axial, limiting the lifespan of these fields probably to less than 50–100 years. A layer of green hydrothermal pyrite-bearing sediment [*Portner et al*., 2012], collected in all cores on the N and E rims of the caldera, and older than about 1200 CE may have accumulated from fall-out of chronic plumes, most likely emanating from within the caldera, during an earlier period of more intense and widespread hydrothermal activity at Axial summit.

[120] The open fissures remaining at the ends of a number of summit eruptions, including both historical eruptions, drained quickly and so avoided being clogged by solidifying lava. This probably occurred as the fissures extended down rift and depressurized the shallowest portion of the

eruptive fissure system. These open fissures were then reused repeatedly by subsequent eruptions as dikes intercepted the open fissures below the surface.

[121] The historical recurrence interval of 13 years between 1998 and 2011 eruptions is statistically identical to the interval we deduce from flows erupted over the last 800 years. Future eruptions are likely to occur within ~15 years and to reuse some of the same fissures that were used in the 1998 and 2011 eruptions in the south caldera and upper south rift.

Acknowledgments

[122] This study could not have been done without the support, hard work, and professionalism of the ships' captains and crews on the R/V *Western Flyer* and the R/V *Zephyr* and the ROV teams for *Tiburon* and *Doc Ricketts*. The dive programs benefitted from the assistance at sea of numerous colleagues and graduate students. The AUV missions in 2006–2008 were conducted off the R/V *Thompson* and the R/V *Atlantis* and their ships' crews were instrumental in successful launches and recoveries of the still developmental AUV. Chief Scientist Jim Holden graciously made the ship time available to us to launch and recover the AUV in 2008. AUV team members Doug Conlin and Duane Thompson assisted with operations during the years of AUV data collection. John Delaney and Deb Kelley kindly provided access to their Simrad EM302 data collected in late summer 2011; the multibeam amplitude data identified the high-backscatter flows on the west flank of the caldera better than in prior data sets. We thank Alicé Davis at MBARI and Robert Oscarson at the U.S. Geological Survey in Menlo Park, and Sarah Roeske, Brian Joy, and Nick Botto at University of California at Davis for assistance with microprobe analyses. DAC, JBP, JFM, DWC, HT, and RAP; collection of the AUV multibeam data in 2006–2008 off the R/V *Thompson* and the R/V *Atlantis* and in 2009 and 2011 off the R/V *Zephyr*; postcruise AUV data processing; and ROV dives using *Tiburon* in 2005 and 2006 and *Doc Ricketts* in 2009 and 2011 off the R/V *Western Flyer* were supported by grants to MBARI from the David and Lucile Packard Foundation. A portion of this work was performed under the auspices of the U.S. Department of Energy by Lawrence Livermore National Laboratory under Contract DE-AC52-07NA27344. Final integration of the sample data with the AUV maps was also supported by NSF grants OCE-1061176 to BMD and OCE-1060515 to DAC and PMEL contribution number 3993.

References

Appelgate, B., and R. W. Embley (1992), Submarine tumuli and inflated tube-fed lava flows on Axial Volcano, Juan de Fuca Ridge, *Bull. Volcanol.*, *54*(6), 447–458.

Baker, E. T., R. E. McDuff, and G. J. Massoth (1990), Hydrothermal venting from the summit of a ridge axis seamount: Axial Volcano, Juan de Fuca Ridge, *J. Geophys. Res.*, *95*, 12,843–12,854.

Ballard, R. D., and T. H. van Andel (1977), Morphology and tectonics of the inner rift valley at 36°50′N on the Mid-Atlantic Ridge, *Geol. Soc. Am. Bull.*, *88*, 507–530.

Ballard, R. D., R. T. Holcomb, and T. H. van Andel (1979), The Galapagos rift at 86°W: 3. Sheet flows, collapse pits, and lava lakes of the rift valley, *J. Geophys. Res.*, *84*, 5407–5422.

Bergmanis, E. C., J. Sinton, and K. H. Rubin (2007), Recent eruptive history and magma reservoir dynamics on the southern East Pacific Rise at 17°30′S, *Geochem. Geophys. Geosyst.*, *8*, Q12O06, doi:10.1029/2007GC001742.

Broecker, W. S., M. Klas, E. Clark, S. Trumbore, G. Bonani, W. Wolfli, and S. Ivy (1990), Accelerator mass spectrometric radiocarbon measurements on foraminifera shells from deep-sea cores: Sample preparation and mass spectrometry, *Radiocarbon*, *32*(2), 119–133.

Butterfield, D. A., K. K. Roe, M. D. Lilley, J. Huber, J. A. Baross, R. W. Embley, and G. J. Massoth (2004), Mixing, reaction and microbial activity in sub-seafloor revealed by temporal and spatial variation in diffuse flow vents at Axial Volcano, in *The Subseafloor Biosphere at Mid-Ocean Ridges, Geophys. Monogr. Ser.*, vol. *144*, edited by W. S. D. Wilcock et al., pp. 269–289, AGU, Washington, D. C.

Caress, D. W., D. A. Clague, J. B. Paduan, W. W. Chadwick Jr., D. A. Butterfield, H. Thomas, D. Conlin, and D. Thompson (2007), AUV mapping of Axial Seamount, Juan de Fuca Ridge: The Northern Caldera floor and Northeast rim, *Eos Trans. AGU*, *88*(52), Fall Meet. Suppl., Abstract T33B-1355.

Caress, D. W., H. Thomas, W. J. Kirkwood, R. McEwen, R. Henthorn, D. A. Clague, C. K. Paull, J. B. Paduan, and K. L. Maier (2008), High-resolution multibeam, sidescan, and subbottom surveys using the MBARI AUV D. Allan B., in *Marine Habitat Mapping Technology for Alaska*, edited by J. R. Reynolds and H. G. Greene, Alaska Sea Grant Coll. Program, Univ. of Alaska, Fairbanks, Alaska, 47–69, doi:10.4027/mhmta.2008.04.

Caress, D. W., D. A. Clague, H. Thomas, D. Thompson, J. B. Paduan, J. F. Martin, and W. W. Chadwick Jr. (2011), *Extent of the 2011 Axial Seamount eruption from repeated 1-m scale bathymetry surveys with the MBARI Mapping AUV, Abstract V11E-2557 presented at 2011 Fall Meeting*, AGU, San Francisco, Calif., 5–9 Dec.

Caress, D. W., D. A. Clague, J. B. Paduan, J. F. Martin, H. Thomas, D. Thompson, C. Nieves-Cardoso, and M. Santa Rosa-del Rio (2012a), *Morphology of the Alarcón rise spreading axis from 1-m resolution AUV bathymetry surveys, Abstract T51B-2566 presented at 2012 Fall Meeting*, AGU, San Francisco, Calif., 3–7 Dec.

Caress, D. W., D. A. Clague, J. B. Paduan, J. F. Martin, B. M. Dreyer, W. W. Chadwick Jr., A. Denny, and D. S. Kelley (2012b), Repeat bathymetric surveys at 1-metre resolution of lava flows erupted at Axial Seamount in April 2011, *Nat. Geosci.*, *5*(7), 483–488, doi:10.1038/NGEO1496.

Chadwick, J., M. Perfit, I. Ridley, I. Jonasson, G. Kamenov, W. W. Chadwick Jr., R. Embley, P. Le Roux, and M. Smith (2005), Magmatic effects of the Cobb hotspot on the Juan de Fuca Ridge, *J. Geophys. Res.*, *110*, B03101, doi:10.1029/2003JB002767.

Chadwick, W., D. Butterfield, R. Embley, V. Tunnicliffe, J. Huber, S. Nooner, and D. A. Clague (2010), Spotlight: Axial Seamount, *Oceanography*, *23*, 38–39.

Chadwick, W. W., Jr. (2003), Quantitative constraints on the growth of submarine lava pillars from a monitoring

instrument that was caught in a lava flow, *J. Geophys. Res.*, *108*(B11), 2534, doi:2510.1029/2003JB002422.

Chadwick, W. W., Jr., and R. W. Embley (1994), Lava flows from a mid-1980s submarine eruption on the cleft segment, Juan de Fuca Ridge, *J. Geophys. Res.*, *99*, 4761–4776.

Chadwick, W. W., Jr., R. W. Embley, and C. G. Fox (1995), Seabeam depth changes associated with recent lava flows, CoAxial segment, Juan de Fuca Ridge: Evidence for multiple eruptions between 1981–1993, *Geophys. Res. Lett.*, *22*, 167–170.

Chadwick, W. W., Jr., R. W. Embley, and T. M. Shank (1998), The 1996 Gorda Ridge eruption: Geologic mapping, sidescan sonar, and SeaBeam comparison results, *Deep Sea Res., Part II*, *45*(12), 2547–2570.

Chadwick, W. W., Jr., T. K. P. Gregg, and R. W. Embley (1999a), Submarine lineated sheet flows: A unique lava morphology formed on subsiding lava ponds, *Bull. Volcanol.*, *61*, 194–206.

Chadwick, W. W., Jr., R. W. Embley, H. B. Milburn, C. Meinig, and M. Stapp (1999b), Evidence for deformation associated with the 1998 eruption of Axial Volcano, Juan de Fuca Ridge, from acoustic extensometer measurements, *Geophys. Res. Lett.*, *26*, 3441–3444.

Chadwick, W. W., Jr., D. S. Scheirer, R. W. Embley, and H. P. Johnson (2001), High-resolution bathymetric surveys using scanning sonars: Lava flow morphology, hydrothermal vents and geologic structure at recent eruption sites on the Juan de Fuca Ridge, *J. Geophys. Res.*, *106*, 16,075–16,100.

Chadwick, W. W., Jr., R. W. Embley, and S. Merle (2002), Emplacement processes of two 1998 lava flows with contrasting morphology, inferred from high-resolution bathymetry and bottom observations at Axial Seamount, Juan de Fuca Ridge, *Eos Trans. AGU*, *83*(4), Ocean Sci. Meet. Suppl., Abstract OS41L-02.

Chadwick, W. W., Jr., S. L. Nooner, D. A. Butterfield, and M. D. Lilley (2012), Seafloor deformation and forecasts of the April 2011 eruption at Axial Seamount, *Nat. Geosci.*, *5*(7), 474–477, doi:10.1038/NGEO1464.

Chadwick, W. W., Jr., et al. (2013) The 1998 eruption at Axial Seamount: New insights on submarine lava flow emplacement from high-resolution mapping, *Geochem. Geophys. Geosyst.*, in press.

Chase, R. L., J. R. Delaney, J. L. Karsten, H. P. Johnson, S. K. Juniper, J. E. Lupton, S. D. Scott, V. Tunnicliffe, S. R. Hammond, and R. E. McDuff (1985), Hydrothermal vents on Axial Seamount on the Juan de Fuca Ridge, *Nature*, *313*, 212–214.

Clague, D. A., and J. B. Paduan (2009), Submarine basaltic volcanism, in *Submarine Volcanism and Mineralization: Modern Through Ancient*, edited by B. Cousens and S. J. Piercey, pp. 41–60, Geol. Assoc. of Can., Short Course 29–30 May 2008, Quebec City, Canada.

Clague, D. A., J. T. Hagstrum, D. E. Champion, D. E., and M. H. Beeson (1999), Kilauea summit overflows: Their ages and distribution in the Puna district, Hawaii, *Bull. Volcanol.*, *61*, 363–381.

Clague, D. A., A. S. Davis, and J. E. Dixon (2003), Submarine strombolian eruptions along the Gorda mid-ocean ridge, in *Explosive Subaequeous Volcanism, Geophys. Monogr. Ser.*, vol. *140*, 379 pp., AGU, Washington, D. C.

Clague, D. A., D. W. Caress, J. B. Paduan, W. W. Chadwick Jr., D. A. Butterfield, H. Thomas, D. Conlin, and D. Thompson (2007), AUV mapping of Axial Seamount, Juan de Fuca Ridge: The southern caldera floor and upper south rift, *Eos Trans. AGU*, *88*(52), Fall Meet. Suppl., Abstract T33B-1354.

Clague, D. A., D. W. Caress, H. Thomas, D. Thompson, M. Calarco, J. Holden, and D. Butterfield (2008), Abundance and distribution of hydrothermal chimneys and mounds on the endeavour ridge determined by 1-m resolution AUV multibeam mapping surveys, *Eos Trans. AGU*, *89*(52), Fall Meet. Suppl., Abstract V41B-2079.

Clague, D. A., J. B. Paduan, and A. S. Davis (2009a), Widespread strombolian eruptions of mid-ocean ridge basalt, *J. Volcanol. Geotherm. Res.*, *180*(2-4), 171–188.

Clague, D. A., J. B. Paduan, R. A. Duncan, J. J. Huard, A. S. Davis, P. Castillo, P. Lonsdale, and A. P. DeVogelaere (2009b), Five million years of episodic alkalic volcanism built Davidson Seamount atop an abandoned spreading center, *Geochem., Geophys., Geosyst.*, *10*, Q12009, doi:10.1029/2009GC002665.

Clague, D. A., J. B. Paduan, B. M. Dreyer, and D. W. Caress (2010), *Lava flow ages and geologic mapping on mid-ocean ridges, Abstract V11A-2236 presented at 2010 Fall Meeting*, AGU, San Francisco, Calif., 13–17 Dec.

Clague, D. A., J. B. Paduan, D. Caress, H. Thomas, W. W. Chadwick Jr., and S. G. Merle (2011a), Volcanic morphology of West Mata Volcano, NE Lau Basin, based on high-resolution bathymetry and depth changes, *Geochem. Geophys. Geosyst.*, *12*, QOAF03, doi:10.1029/2011GC003791.

Clague, D. A., J. B. Paduan, B. M. Dreyer, D. W. Caress, and J. F. Martin (2011b), *High-resolution AUV mapping and lava flow ages at Axial Seamount, Abstract V14C-05 presented at 2011 Fall Meeting*, AGU, San Francisco, Calif., 5–9 Dec.

Clague, D. A., et al. (2012), *Geology of the Alarcon Rise based on 1-m resolution bathymetric maps and ROV observations and sampling, Abstract T44A-04 presented at 2012 Fall Meeting*, AGU, San Francisco, Calif., 3–7 Dec.

Colman, A., et al. (2012), Effects of variable magma supply on mid-ocean ridge eruptions: Costraints from mapped lava flows along the Galapagos Spreading Center, *Geochem. Geophys. Geosyst.*, *13*, Q08014, doi:10.1029/2012GC004163.

Cormier, M.-H., W. B. F. Ryan, A. K. Shah, W. Jin, A. M. Bradley, and D. R. Yoerger (2003), Waxing and waning volcanism along the East Pacific Rise on a millennium time scale, *Geology*, *31*(7), 633–636.

Crane, K., and R. D. Ballard (1981), Volcanics and structure of the famous Narrowgate Rift: Evidence for cyclic evolution: AMAR 1, *J. Geophys. Res.*, *86*, 5112–5124.

Desonie, D. L., and R. A. Duncan (1990), The Cobb-Eickelberg seamount chain: Hotspot volcanism with mid-ocean ridge basalt affinity, *J. Geophys. Res.*, *95*, 12,697–12,712.

Dreyer, B. M., D. A. Clague, and J. B. Gill (2013), Petrologic variability of recent magmatism at Axial Seamount summit, Juan de Fuca Ridge, *Geochemistry, Geophysics, Geosystem.*

Dziak, R. P., and C. G. Fox (1999), The January 1998 earthquake swarm at Axial Volcano Juan de Fuca Ridge: Hydroacoustic evidence of seafloor volcanic activity, *Geophys. Res. Lett.*, *26*, 3429–3432.

Dziak, R. P., J. H. Haxel, D. R. Bohnenstiehl, W. W. Chadwick Jr., S. L. Nooner, M. J. Fowler, H. Matsumoto, and D. A. Butterfield (2012), Seismic precursors and magma ascent before the April 2011 eruption at Axial Seamount, *Nat. Geosci.*, *5*(7), 478–482, doi:10.1038/NGEO1490.

Embley, R. W., and W. W. Chadwick Jr. (1994), Volcanic and hydrothermal processes associated with a recent phase of seafloor spreading at the northern Cleft segment: Juan de Fuca Ridge, *J. Geophys. Res.*, *99*, 4741–4760.

Embley, R. W., K. M. Murphy, and C. G. Fox (1990), High resolution studies of the summit of Axial Volcano, *J. Geophys. Res.*, *95*, 12,785–12,812.

Embley, R. W., W. W. Chadwick Jr., M. R. Perfit, and E. T. Baker (1991), Geology of the Northern Cleft segment, Juan de Fuca Ridge: Recent lava flows, sea-floor spreading, and the formation of megaplumes, *Geology*, *19*, 771–775.

Embley, R. W., W. W. Chadwick Jr., I. R. Jonasson, D. A. Butterfield, and E. T. Baker (1995), Initial results of the rapid response to the 1993 CoAxial event: Relationships between hydrothermal and volcanic processes, *Geophys. Res. Lett.*, *22*, 143–147.

Embley, R. W., W. W. Chadwick Jr., D. A. Clague, and D. Stakes (1999), The 1998 eruption of axial volcano: Multibeam anomalies and seafloor observations, *Geophys. Res. Lett.*, *26*, 3425–2428.

Embley, R. W., W. W. Chadwick Jr., M. R. Perfit, M. C. Smith, and J. R. Delaney (2000), Recent eruptions on the CoAxial segment of the Juan de Fuca Ridge: Implications for mid-ocean ridge accretion processes, *J. Geophys. Res.*, *105*, 16,501–16,525.

Engels, J. L., M. H. Edwards, D. J. Fornari, M. R. Perfit, and J. R. Cann (2003), A new model for submarine volcanic collapse formation, *Geochem. Geophys. Geosyst.*, *4*(9), 1077, doi:10.1029/2002GC000483.

Ferrini, V. L., D. J. Fornari, T. M. Shank, J. C. Kinsey, M. A. Tivey, S. A. Soule, S. M. Carbotte, L. L. Whitcomb, D. Yoerger, and J. Howland (2007), Submeter bathymetric mapping of volcanic and hydrothermal features on the East Pacific Rise crest at 9°50′N, *Geochem. Geophys. Geosyst.*, *8*, Q01006, doi:01010.01029/02006GC001333.

Fornari, D. J. (1986), Submarine lava tubes and channels, *Bull. Volcanol.*, *48*, 291–298.

Fornari, D. J., et al. (2004), Submarine lava flow emplacement at the East Pacific Rise 9°50′N: Implications for uppermost ocean crust stratigraphy and hydrothermal fluid circulation, in *Mid-Ocean Ridges: Hydrothermal Interactions Between the Lithosphere and Oceans, Geophys. Monogr. Ser.*, vol. *148*, edited by C. R. German, J. Lin, and L. M. Parson, pp. 187–217, AGU, Washington, D. C.

Fornari, D. J., et al. (2012), The East Pacific Rise between 9°N and 10°N: Twenty-five years of integrated, multidisciplinary oceanic spreading center studies, *Oceanography*, *25*(1), 18–43, doi:10.5670/oceanog.2012.02.

Fox, C. G. (1999), In situ ground deformation measurements from the summit of Axial Volcano during the 1998 volcanic episode, *Geophys. Res. Lett.*, *26*, 3437–3440.

Fox, C. G., W. W. Chadwick Jr., and R. W. Embley (1992), Detection of changes in ridge-crest morphology using repeated multibeam sonar surveys, *J. Geophys. Res.*, *97*, 11,149–11,162.

Fundis, A. T., S. A. Soule, D. J. Fornari, and M. R. Perfit (2010), Paving the seafloor: Volcanic emplacement processes during the 2005–2006 eruptions at the fast spreading East Pacific Rise, 9°50′N, *Geochem. Geophys. Geosyst.*, *11*, Q08024, doi:10.1029/2010GC003058.

Goldstein, S. J., M. T. Murrell, D. R. Janecky, J. R. Delaney, and D. A. Clague (1992), Geochronology and petrogenesis of MORB from the Juan de Fuca and Gorda ridges by 238 U-230Th disequilibrium, *Earth Planet. Sci. Lett.*, *109*(1-2), 255–272.

Goss, A. R., M. R. Perfit, W. I. Ridley, K. H. Rubin, G. D. Kamenov, S. A. Soule, A. Fundis, and D. J. Fornari (2010), Geochemistry of lavas from the 2005–2006 eruption at the East Pacific Rise, 9°46′N- 9°56′N: Implications for ridge crest plumbing and decadal changes in magma chamber compositions, *Geochem. Geophys. Geosyst.*, *11*, Q05T09, doi:10.1029/2009GC002977.

Gregg, T. K. P., and W. W. Chadwick Jr. (1996), Submarine lava-flow inflation: A model for the formation of lava pillars, *Geology*, *24*(11), 981–984.

Gregg, T. K. P., and J. H. Fink (1995), Quantification of submarine lava-flow morphology through analog experiments, *Geology*, *23*(1), 73–76.

Gregg, T. K. P., and J. H. Fink (2000), A laboratory investigation into the effects of slope on lava flow morphology, *J. Volcanol. Geotherm. Res.*, *96*(3-4), 145–159.

Gregg, T. K. P., and D. K. Smith (2003), Volcanic investigations of the Puna Ridge, Hawaii: Relations of lava flow morphologies and underlying slopes, *J. Volcanol. Geotherm. Res.*, *126*, 63–77.

Gregg, T. K. P., D. J. Fornari, M. R. Perfit, R. M. Haymon, and J. H. Fink (1996), Rapid emplacement of a mid-ocean ridge lava flow on the East Pacific Rise at 9°46′-51′N, *Earth Planet. Sci. Lett.*, *144*, E1–E7.

Griffiths, R. W., and J. H. Fink (1992), Solidification and morphology of submarine lavas: A dependence on extrusion rate, *J. Geophys. Res.*, *97*, 19,729–19,737.

Haymon, R. M., et al. (1993), Volcanic eruption of the mid-ocean ridge along the East Pacific Rise crest at 9°45–52′N: Direct submersible observations of seafloor phenomena associated with an eruption event in April 1991, *Earth Planet. Sci. Lett.*, *119*, 85–101.

Head, J. W., III, and L. Wilson (2003), Deep submarine pyroclastic eruptions: Theory and prdicted landforms and deposits, *J. Volcanol. Geotherm. Res.*, *121*, 155–193.

Helo, C., M. A. Longpre, N. Shimizu, D. A. Clague, and J. Stix (2011), Explosive eruptions at mid-ocean ridges driven by CO2-rich magmas, *Nat. Geosci.*, *4*(4), 260–263.

Holcomb, R. T. (1987), Eruptive history and long-term behavior of Kilauea Volcano, in *Volcanism in Hawaii, U.S. Geol. Surv. Prof. Pap.*, vol. *1350*, edited by R. W. Decker, T. L. Wright, and P. H. Stauffer, United States Government Printing Office, Washington, pp. 261–350.

Holcomb, R. T., J. G. Moore, P. W. Lipman, and R. H. Balderson (1988), Voluminous submarine lava flows from Hawaiian volcanoes, *Geology*, *16*(5), 400–404.

Hon, K., J. Kauahikaua, R. Denlinger, and K. Mackay (1994), Emplacement and inflation of pahoehoe sheet flows: Observations and measurements of active lava flows on Kilauea volcano, Hawaii, *Geol. Soc. Am. Bull.*, *106*, 351–370.

Johnson, H. P., and R. W. Embley (1990), Axial Seamount: An active ridge axis volcano on the central Juan de Fuca Ridge, *J. Geophys. Res.*, *95*, 12,689–12,696.

Karsten, J. L., and J. R. Delaney (1989), Hot spot-ridge crest convergence in the Northeast Pacific, *J. Geophys. Res.*, *94*, 700–712.

Lockwood, J. P., and P. L. Lipman (1987), Holocene eruptive history of Mauna Loa Volcano, in *Volcanism in Hawaii, U.S. Geol. Surv. Prof. Pap.*, vol. *1350*, edited by R. W. Decker, T. L. Wright, and P. H. Stauffer, United States Government Printing Office, Washington, pp. 537–570.

Lockwood, J. P., J. J. Dvorak, T. T. English, R. Y. Koyanagi, A. T. Okamura, M. J. Summers, and W. F. Tanigawa (1987), Mauna Loa 1974–1984: A decade of intrusive and extrusive activity, in *Volcanism in Hawaii, U.S. Geol. Surv. Prof. Pap.*, vol. *1350*, edited by R. W. Decker, T. L. Wright, and P. H. Stauffer, United States Government Printing Office, Washington, pp. 537–570.

Macdonald, G. A. (1965), Hawaiian calderas, *Pac. Sci.*, *19*, 320–334.

Martin J. F., P. L. Clark, D. A. Clague, D. W. Caress, R. A. Portner, J. B. Paduan, B. M. Dreyer (2012), Effect of melt composition and crystal content on flow morphology along the Alarcón Rise, Mexico, Abstract T51B-2571, Presented at Fall AGU Meeting, San Francisco, Dec. 3–7.

Moore, J. G. (1975), Mechanism of formation of pillow lava, *Am. Sci.*, *63*, 269–277.

Neal, C. A., and J. P. Lockwood (2003), Geologic Map of the Summit Region of Kilauea Volcano, Hawaii, Geol. Invest. Ser. I-2759, sheet 1, U.S. Geol. Surv., United States Government Printing Office, Washington.

Nooner, S. L., and W. W. Chadwick Jr. (2009), Volcanic inflation measured in the caldera of Axial Seamount: Implications for magma supply and future eruptions, *Geochem. Geophys. Geosyst.*, *10*, Q02002, doi:10.1029/2008GC002315.

Paduan, J. B., D. A. Clague, A. S. Davis, W. W. Chadwick Jr., B. L. Cousens, and R. W. Embley (2005), Large lava pond complex on the Juan de Fuca Ridge: An effusive, energetic eruption that drained away, *Eos Trans. AGU*, *86*(52), Fall Meet. Suppl., Abstract V51C-1511.

Paduan, J. B., D. A. Clague, D. W. Caress, H. Thomas, D. Thompson, and D. Conlin (2009), High-resolution AUV mapping reveals structural details of submarine inflated lava flows, *Eos Trans. AGU*, *90*(52), Fall Meet. Suppl., Abstract V51D-1732.

Paduan, J. B., D. A. Clague, and D. W. Caress (2012a), Lava ponds on south rift of Axial Seamount: AUV mapping reveals elaborate, extensive complex, poster B0783 presented at the 2012 Ocean Sciences Meeting, Salt Lake City, Utah, 20–24 Feb.

Paduan, J. B., D. A. Clague, D. W. Caress, L. Lundsten, J. F. Martin, and C. Nieves-Cardoso (2012b), *Newly discovered hydrothermal system on the Alarcón Rise, Mexico, Abstract T51B-2572 presented at 2012 Fall Meeting*, AGU, San Francisco, Calif., 3–7 Dec.

Perfit, M. R., and W. W. Chadwick Jr. (1998), Magmatism at mid-ocean ridges: Constraints from volcanological and geochemical investigations, in *Faulting and Magmatism at Mid-Ocean Ridges, Geophys. Monogr. Ser.*, vol. *106*, edited by W. R. Buck et al., pp. 59–116, AGU, Washington, D. C.

Peterson, D. W., R. T. Holcomb, R. I. Tilling, and R. L. Christiansen (1994), Development of lava tubes in the light of observations at Mauna Ulu, Kilauea Volcano, Hawaii, *Bull. Volcanol.*, *56*, 343–360.

Portner, R. A., D. A. Clague, J. B. Paduan, and J. M. Martin (2012), *Competing styles of deep-marine explosive eruptions revealed from Axial Seamount and Juan De Fuca ridge push-core records, Abstract V21A-2751 presented at 2012 Fall Meeting*, AGU, San Francisco, Calif., 3–7 Dec.

Rubin K. H., and J. D. Macdougall (1990), A radioactive decay technique for dating neovolcanic MORB, *Earth Planet. Sci. Lett.*, *101*, 313–322.

Rubin, K. H., I. Van der Zander, M. C. Smith, and E. C. Bergmanis (2005), Minimum speed limit for ocean ridge magmatism from 210Pb-226Ra-230Th disequilibria, *Nature*, *437*(7058), 534–538.

Rubin, K. H., S. A. Soule, W. W. Chadwick Jr, D. J. Fornari, D. A. Clague, R. W. Embley, E. T. Baker, M. R. Perfit, D. W. Caress, and R. P. Dziak (2012), Volcanic eruptions in the deep sea, *Oceanography*, *25*(1), 142–157.

Rubin, M., J. P. Lockwood, and I. Friedman (1987), Hawaiian radiocarbon dates, in *Volcanism in Hawaii, U.S. Geol. Surv. Prof. Pap.*, vol. *1350*, edited by R. W. Decker, T. L. Wright, and P. H. Stauffer, United States Government Printing Office, Washington, pp. 213–242.

Shaw, H. R. (1972), Viscosities of magmatic silicate liquids: An empirical method of prediction, *Am. J. Sci.*, *272*, 870–893.

Simkin, T., and K. A. Howard (1970), Caldera collapse in the Galapagos Islands, 1968, *Science*, *169*(3944), 429–437.

Sinton, J. M., E. Bergmanis, K. Rubin, R. Batiza, T. K. P. Gregg, K. Gronvold, K. C. Macdonald, and S. M. White (2002), Volcanic eruptions on mid-ocean ridges: New evidence from the superfast spreading East Pacific Rise, 17°-19°S, *J. Geophys. Res.*, *107*(B6), 2115, doi:10.1029/2000JB000090.

Sohn, R. A., et al. (2008), Explosive volcanism on the ultraslow-spreading Gakkel Ridge, Arctic Ocean, *Nature*, *453*, 1236–1238, doi:10.1038/nature07075.

Soule, S. A., D. J. Fornari, M. R. Perfit, M. A. Tivey, W. Ridley, and H. Schouten (2005), Channelized lava flows at the East Pacific Rise crest 9°–10°N: The importance of off-axis lava transport in developing the architecture of young oceanic crust, *Geochem. Geophys. Geosyst.*, *6*, Q08005, doi:10.1029/2005GC000912.

Soule, S. A., D. J. Fornari, M. R. Perfit, and K. H. Rubin (2007), New insights into mid-ocean ridge volcanic processes from the 2005–2006 eruption of the East Pacific Rise, 9°46′N–9°56′N, *Geology*, *35*(12), 1079–1082.

Soule, S. A., J. Escartin, and D. J. Fornari (2009), A record of eruption and intrusion at a fast spreading ridge axis: Axial summit trough of the East Pacific Rise at 9–10°, *Geochem. Geophys. Geosyst.*, *10*, Q10T07, doi:10.1029/2008GC002354.

Stuiver, M., and T. F. Braziunas (1993), Modeling atmospheric 14C influences and 14C ages of marine samples to 10 000 BC, *Radiocarbon*, *35*(1), 137–189.

Stuiver, M., and P. J. Reimer (1993), Extended 14C data base and revised CALIB 3.0 14C age calibration programme, *Radiocarbon*, *35*(1), 215–231.

Swanson, D. A., T. R. Rose, R. S. Fiske, and J. P. McGeehan (2012), Keanakakoi tephra produced by 300 years of explosive eruptions following collapse of Kilauea's caldera in about 1500 CE, *J. Volcanol. Geotherm. Res.*, *215–216*, 8–25.

Van Andel, T. H., and P. D. Komar (1969), Ponded sediments of the Mid-Atlantic Ridge between 22° and 23° North Latitude, *Geol. Soc. Am. Bull.*, *80*(7), 1163–1190, doi:10.1130/0016–7606(1969)80[1163:PSOTMR]2.0.CO;2.

Volpe, A. M., and S. J. Goldstein (1993), 226Ra-230Th disequilibrium in axial and off-axis mid-ocean ridge basalts, *Geochim. Cosmoschim. Acta*, *57*(6), 1233–1241.

Walker, G. P. L. (1991), Structure, and origin by injection of lava under surface crust, of tumuli, ''lava rises,'' ''lava rise-pits,'' and ''lava inflation clefts'' in Hawaii, *Bull. Volcanol.*, *53*, 546–558.

White, S. M., K. C. Macdonald, and R. M. Haymon (2000), Basaltic lava domes, lava lakes, and volcanic segmentation on the southern East Pacific Rise, *J. Geophys. Res.*, *103*, 25,519–25,536.

White, S. M., J. D. Meyer, R. M. Haymon, K. C. Macdonald, E. T. Baker, and J. A. Resing (2008), High-resolution surveys along the hot spot-affected Galapagos Spreading Center: 2. Influence of magma supply on volcanic morphology, *Geochem. Geophys. Geosyst.*, *9*, Q09004, doi:10.1029/2008GC002036.

Yoerger, D. R., A. M. Bradley, M. Jakuba, M. A. Tivey, C. R. German, T. M. Shank, and R. W. Embley (2007), Mid-ocean

ridge exploration with an autonomous underwater vehicle, *Oceanography*, *20*, 53–59.

Zonenshain, L. P., M. I. Kuzmin, Y. A. Bogdanov, A. P. Lisitsin, and A. M. Podrazhansky (1989), Geology of the Axial Seamount, Juan de Fuca Spreading Center, Northeastern Pacific, in *Evolution of Mid Ocean Ridges, Geophys. Monogr. Ser.*, vol. 57, edited by J. M. Sinton, pp. 53–63, AGU, Washington, D. C.